# Structural insights into Cullin4-RING ubiquitin ligase remodelling by Vpr from simian immunodeficiency viruses

Sofia Banchenko[1¶], Ferdinand Krupp[1¶], Christine Gotthold[1], Jörg Bürger[1,2], Andrea Graziadei[3], Francis O'Reilly[3], Ludwig Sinn[3], Olga Ruda[1], Juri Rappsilber[3,4], Christian M. T. Spahn[1], Thorsten Mielke[2], Ian A. Taylor[5], David Schwefel[1*]

[1] Institute of Medical Physics and Biophysics, Charité – Universitätsmedizin Berlin, corporate member of Freie Universität Berlin, Humboldt-Universität zu Berlin, and Berlin Institute of Health, Berlin, Germany

[2] Microscopy and Cryo-Electron Microscopy Service Group, Max-Planck-Institute for Molecular Genetics, Berlin, Germany

[3] Bioanalytics Unit, Institute of Biotechnology, Technische Universität Berlin, Berlin, Germany

[4] Wellcome Centre for Cell Biology, University of Edinburgh, Edinburgh, United Kingdom

[5] Macromolecular Structure Laboratory, The Francis Crick Institute, London, United Kingdom

*Corresponding author

E-mail: david.schwefel@charite.de (DS)

[¶]These authors contributed equally to this work

# Abstract

Viruses have evolved means to manipulate the host's ubiquitin-proteasome system, in order to down-regulate antiviral host factors. The Vpx/Vpr family of lentiviral accessory proteins usurp the substrate receptor DCAF1 of host Cullin4-RING ligases (CRL4), a family of modular ubiquitin ligases involved in DNA replication, DNA repair and cell cycle regulation. $CRL4^{DCAF1}$ specificity modulation by Vpx and Vpr from certain simian immunodeficiency viruses (SIV) leads to recruitment, poly-ubiquitylation and subsequent proteasomal degradation of the host restriction factor SAMHD1, resulting in enhanced virus replication in differentiated cells. To unravel the mechanism of SIV Vpr-induced SAMHD1 ubiquitylation, we conducted integrative biochemical and structural analyses of the Vpr protein from SIVs infecting *Cercopithecus cephus* ($SIV_{mus}$). X-ray crystallography reveals commonalities between $SIV_{mus}$ Vpr and other members of the Vpx/Vpr family with regard to DCAF1 interaction, while cryo-electron microscopy and cross-linking mass spectrometry highlight a divergent molecular mechanism of SAMHD1 recruitment. In addition, these studies demonstrate how $SIV_{mus}$ Vpr exploits the dynamic architecture of the multi-subunit $CRL4^{DCAF1}$ assembly to optimise SAMHD1 ubiquitylation. Together, the present work provides detailed molecular insight into variability and species-specificity of the evolutionary arms race between host SAMHD1 restriction and lentiviral counteraction through Vpx/Vpr proteins.

## Author summary

Due to the limited size of virus genomes, virus replication critically relies on host cell components. In addition to the host cell's energy metabolism and its DNA replication and protein synthesis apparatus, the protein degradation machinery is an attractive target for viral re-appropriation. Certain viral factors divert the specificity of host ubiquitin ligases to antiviral host factors, in order to mark them for destruction by the proteasome, to lift intracellular barriers to virus replication. Here, we present molecular details of how the simian immunodeficiency virus accessory protein Vpr interacts with a substrate receptor of host Cullin4-RING ubiquitin ligases, and how this interaction redirects the specificity of Cullin4-RING to the antiviral host factor SAMHD1. The studies uncover the mechanism of Vpr-induced SAMHD1 recruitment and subsequent ubiquitylation. Moreover, by comparison to related accessory proteins from other immunodeficiency virus species, we illustrate the surprising variability in the molecular strategies of SAMHD1 counteraction, which these viruses adopted during evolutionary adaptation to their hosts. Lastly, our work also provides deeper insight into the inner workings of the host's Cullin4-RING ubiquitylation machinery.

52 # Introduction

53 A large proportion of viruses have evolved means to co-opt their host's ubiquitylation machinery, in
54 order to improve replication conditions, either by introducing viral ubiquitin ligases and deubiquitinases,
55 or by modification of host proteins involved in ubiquitylation [1-3]. In particular, host ubiquitin ligases
56 are a prominent target for viral usurpation, to redirect specificity towards antiviral host restriction
57 factors. This results in recruitment of restriction factors as non-endogenous *neo*-substrates, inducing
58 their poly-ubiquitylation and subsequent proteasomal degradation [4-8]. This counteraction of the host's
59 antiviral repertoire is essential for virus infectivity and spread [9-12], and mechanistic insights into these
60 specificity changes extend our understanding of viral pathogenesis and might pave the way for novel
61 treatments.

62 Frequently, virally encoded modifying proteins associate with, and adapt the Cullin4-RING ubiquitin
63 ligases (CRL4) [5]. CRL4 consists of a Cullin4 (CUL4) scaffold that bridges the catalytic RING-domain
64 subunit ROC1 to the adaptor protein DDB1, which in turn binds to exchangeable substrate receptors
65 (DCAFs, DDB1- and CUL4-associated factors) [13-17]. In some instances, the DDB1 adaptor serves as
66 an anchor for virus proteins, which then act as "viral DCAFs" to recruit the antiviral substrate. Examples
67 are the simian virus 5 V protein and mouse cytomegalovirus M27, which bind to DDB1 and recruit
68 STAT1/2 proteins for ubiquitylation, in order to interfere with the host's interferon response [18-20].
69 Similarly, CUL4-dependent downregulation of STAT signalling is important for West Nile Virus
70 replication [21]. In addition, the hepatitis B virus X protein hijacks DDB1 to induce proteasomal
71 destruction of the structural maintenance of chromosome (SMC) complex to promote virus replication
72 [22, 23].

73 Viral factors also bind to and modify DCAF receptors in order to redirect them to antiviral substrates.
74 Prime examples are the lentiviral accessory proteins Vpr and Vpx. All contemporary human and simian
75 immunodeficiency viruses (HIV/SIV) encode Vpr, while only two lineages, represented by HIV-2 and
76 SIV infecting mandrills, carry Vpx [24]. Vpr and Vpx proteins are packaged into progeny virions and
77 released into the host cell upon infection, where they bind to DCAF1 in the nucleus [25]. In this work,
78 corresponding simian immunodeficiency virus Vpx/Vpr proteins will be indicated with their host
79 species as subscript, with the following abbreviations used: mus – moustached monkey (*Cercopithecus*

80 *cephus*), mnd – mandrill (*Mandrillus sphinx*), rcm – red-capped mangabey (*Cercocebus torquatus*), sm
81 – sooty mangabey (*Cercocebus atys*), deb – De Brazza's monkey (*Cercopithecus neglectus*), syk –
82 Syke's monkey (*Cercopithecus albogularis*), agm – african green monkey (*Chlorocebus* spec).
83 $Vpr_{HIV-1}$ is important for virus replication *in vivo* and in macrophage infection models [26]. Recent
84 proteomic analyses revealed that DCAF1 specificity modulation by $Vpr_{HIV-1}$ proteins results in down-
85 regulation of hundreds of host proteins in a DCAF1- and proteasome-dependent manner [27], including
86 the previously reported $Vpr_{HIV-1}$ degradation targets UNG2 [28], HLTF [29], MUS81 [30, 31], MCM10
87 [32] and TET2 [33]. This surprising promiscuity in degradation targets is also partially conserved in
88 more distant clades exemplified by $Vpr_{agm}$ and $Vpr_{mus}$ [27]. However, Vpr pleiotropy, and the lack of
89 easily accessible experimental models, have prevented a characterisation of how these degradation
90 events precisely promote replication [26].
91 By contrast, Vpx, exhibits a much narrower substrate range. It has recently been reported to target
92 stimulator of interferon genes (STING) and components of the human silencing hub (HUSH) complex
93 for degradation, leading to inhibition of antiviral cGAS-STING-mediated signalling and reactivation of
94 latent proviruses, respectively [34-36]. Importantly, Vpx also recruits the SAMHD1 restriction factor to
95 DCAF1, in order to mark it for proteasomal destruction [37, 38]. SAMHD1 is a deoxynucleotide
96 triphosphate (dNTP) triphosphohydrolase that restricts retroviral replication in non-dividing cells by
97 lowering the dNTP pool to levels that cannot sustain viral reverse transcription [39-46]. Retroviruses
98 that express Vpx are able to alleviate SAMHD1 restriction, allowing for replication in differentiated
99 myeloid lineage cells, resting T cells and memory T cells [38, 47, 48]. As a result of the constant
100 evolutionary arms race between the host's SAMHD1 restriction and its viral antagonist Vpx, the
101 mechanism of Vpx-mediated SAMHD1 recruitment is highly virus species- and strain-specific: The
102 Vpx clade represented by $Vpx_{HIV-2}$ recognises the SAMHD1 C-terminal domain (CtD), while $Vpx_{mnd2/rcm}$
103 binds the SAMHD1 N-terminal domain (NtD) in a fundamentally different way [24, 49-52].
104 In the course of evolutionary adaptation to their primate hosts, and due to selective pressure to evade
105 SAMHD1 restriction, two groups of SIVs that do not have Vpx, $SIV_{agm}$, and $SIV_{deb/mus/syk}$, *neo*-
106 functionalised their Vpr to bind SAMHD1 and induce its degradation [24, 49, 53]. Consequently, these

107 species evolved "hybrid" Vpr proteins that retain targeting of some host factors depleted by HIV-1-type
108 Vpr [27], and additionally induce SAMHD1 degradation.
109 To uncover the molecular mechanisms of DCAF1- and SAMHD1-interaction of such a "hybrid" Vpr,
110 we initiated integrative biochemical and structural analyses of the Vpr protein from an SIV infecting
111 *Cercopithecus cephus*, $Vpr_{mus}$. These studies reveal similarities and differences to Vpx and Vpr proteins
112 from other lentivirus species and pinpoint the divergent molecular mechanism of $Vpr_{mus}$-dependent
113 SAMHD1 recruitment to CUL4/ROC1/DDB1/DCAF1 ($CRL4^{DCAF1}$). Furthermore, cryo-electron
114 microscopic (cryo-EM) reconstructions of a $Vpr_{mus}$-modified $CRL4^{DCAF1}$ protein complex allow for
115 insights into the structural plasticity of the entire CRL4 ubiquitin ligase assembly, with implications for
116 the ubiquitin transfer mechanism.
117

118 # Results

119 ## SAMHD1-CtD is necessary and sufficient for $Vpr_{mus}$-binding and ubiquitylation in vitro

120 To investigate the molecular interactions between $Vpr_{mus}$, the *neo*-substrate SAMHD1 from rhesus
121 macaque and CRL4 subunits DDB1/DCAF1 C-terminal domain (DCAF1-CtD), protein complexes were
122 reconstituted *in vitro* from purified components and analysed by gel filtration (GF) chromatography.
123 The different protein constructs that were employed are shown schematically in S1A Fig. In the absence
124 of additional binding partners, $Vpr_{mus}$ is insoluble after removal of the GST affinity purification tag (S1B
125 Fig) and accordingly could not be applied to the GF column. No interaction of SAMHD1 with
126 DDB1/DCAF1-CtD could be detected in the absence of $Vpr_{mus}$ (S1C Fig). Analysis of binary protein
127 combinations ($Vpr_{mus}$ and DDB1/DCAF1-CtD; $Vpr_{mus}$ and SAMHD1) shows that $Vpr_{mus}$ elutes together
128 with DDB1/DCAF1-CtD (S1D Fig) or with SAMHD1 (S1E Fig). Incubation of $Vpr_{mus}$ with
129 DDB1/DCAF1B and SAMHD1 followed by GF resulted in co-elution of all three components (Fig 1A).
130 Together, these results show that $Vpr_{mus}$ forms stable binary and ternary protein complexes with
131 DDB1/DCAF1-CtD and/or SAMHD1 *in vitro*. Furthermore, incubation with any of these interaction
132 partners apparently stabilises $Vpr_{mus}$ by alleviating its tendency for aggregation/insolubility.
133 Previous cell-based assays indicated that residues 583-626 of rhesus macaque SAMHD1 (SAMHD1-
134 CtD) are necessary for $Vpr_{mus}$-induced proteasomal degradation [49]. To test this finding in our *in vitro*

135 system, constructs containing SAMHD1-CtD fused to T4 lysozyme (T4L-SAMHD1-CtD), or
136 containing only the N-terminal domains of SAMHD1, and lacking SAMHD1-CtD (SAMHD1-ΔCtD),
137 were incubated with $Vpr_{mus}$ and DDB1/DCAF1-CtD, and complex formation was assessed by GF
138 chromatography. Analysis of the resulting chromatograms by SDS-PAGE shows that SAMHD1-ΔCtD
139 did not co-elute with DDB1/DCAF1-CtD/$Vpr_{mus}$ (Fig 1B). By contrast, T4L-SAMHD1-CtD
140 accumulated in the same elution peak as DDB1/DCAF1-CtD and $Vpr_{mus}$ (Fig 1C). These results confirm
141 that SAMHD1-CtD is necessary for stable association with DDB1/DCAF1-CtD/$Vpr_{mus}$ *in vitro*, and
142 demonstrate that SAMHD1-CtD is sufficient for $Vpr_{mus}$-mediated recruitment of the T4L-SAMHD1-
143 CtD fusion construct to DDB1/DCAF1-CtD.
144 To correlate these data with enzymatic activity, *in vitro* ubiquitylation assays were conducted by
145 incubating SAMHD1, SAMHD1-ΔCtD or T4L-SAMHD1-CtD with purified $CRL4^{DCAF1-CtD}$, E1
146 (UBA1), E2 (UBCH5C), ubiquitin and ATP. Input proteins are shown in S2A Fig, and control reactions
147 in S2B, C Fig. In the absence of $Vpr_{mus}$, no SAMHD1 ubiquitylation was observed (Figs 1D and S2D),
148 while addition of $Vpr_{mus}$ resulted in robust SAMHD1 ubiquitylation, as demonstrated by an upward shift
149 of SAMHD1 in the SDS PAGE analysis, induced by covalent modification with increasingly more
150 ubiquitin molecules, leading to almost complete loss of the band corresponding to unmodified SAMHD1
151 after 15 min incubation (Figs 1E and S2E). In agreement with the analytical GF data, SAMHD1-ΔCtD
152 was not ubiquitylated in the presence of $Vpr_{mus}$ (Figs 1F and S2F). By contrast, T4L-SAMHD1-CtD was
153 efficiently ubiquitylated, resulting in >90% loss of the band corresponding to unmodified T4L-
154 SAMHD1-CtD after 15 min (Figs 1G and S2F). Again, these data substantiate the functional importance
155 of SAMHD1-CtD for $Vpr_{mus}$-mediated recruitment to the $CRL4^{DCAF1}$ ubiquitin ligase.
156

157 **Crystal Structure analysis of apo- and $Vpr_{mus}$-bound DDB1/DCAF1-CtD protein**
158 **complexes**

159 To obtain structural information regarding $Vpr_{mus}$ and its mode of binding to the CRL4 substrate receptor
160 DCAF1, the X-ray crystal structures of a DDB1/DCAF1-CtD complex, and DDB1/DCAF1-CtD/T4L-
161 $Vpr_{mus}$ (residues 1-92) fusion protein ternary complex were determined. The structures were solved
162 using molecular replacement and refined to resolutions of 3.1 Å and 2.5 Å respectively (S1 Table).

163 $Vpr_{mus}$ adopts a three-helix bundle fold, stabilised by coordination of a zinc ion by His and Cys residues
164 on Helix-1 and at the C-terminus (Fig 2A). Superposition of $Vpr_{mus}$ with previously determined $Vpx_{sm}$
165 [50], $Vpx_{mnd2}$ [51, 52], and $Vpr_{HIV-1}$ [54] structures reveals a conserved three-helix bundle fold, and
166 similar position of the helix bundles on DCAF1-CtD (S3A Fig). In addition, the majority of side chains
167 involved in DCAF1-interaction are type-conserved in all Vpx and Vpr proteins (Figs S3B-G and S6A),
168 strongly suggesting a common molecular mechanism of host CRL4-DCAF1 hijacking by the Vpx/Vpr
169 family of accessory proteins. However, there are also significant differences in helix length and register
170 as well as conformational variation in the loop region N-terminal of Helix-1, at the start of Helix-1 and
171 in the loop between Helices-2 and -3 (S3A Fig).
172 $Vpr_{mus}$ binds to the side and on top of the disk-shaped 7-bladed β-propeller (BP) DCAF1-CtD domain
173 with a total contact surface area of ~1600 $Å^2$ comprising three major regions of interaction. The extended
174 $Vpr_{mus}$ N-terminus attaches to the cleft between DCAF1 BP blades 1 and 2 through several hydrogen
175 bonds, electrostatic and hydrophobic interactions (S3B-D Fig). A second, smaller contact area is formed
176 by hydrophobic interaction between $Vpr_{mus}$ residues L31 and E34 from Helix-1, and DCAF1 W1156,
177 located in a loop on top of BP blade 2 (S3E Fig). The third interaction surface comprises the C-terminal
178 half of $Vpr_{mus}$ Helix-3, which inserts into a ridge on top of DCAF1 (S3F, G Fig).
179 Superposition of the apo-DDB1/DCAF1-CtD and $Vpr_{mus}$-bound crystal structures reveals
180 conformational changes in DCAF1 upon $Vpr_{mus}$ association. Binding of the N-terminal arm of $Vpr_{mus}$
181 induces only a minor rearrangement of a loop in BP blade 2 (S3C Fig). By contrast, significant structural
182 changes occur on the upper surface of the BP domain: polar and hydrophobic interactions of DCAF1
183 residues P1329, F1330, F1355, N1371, L1378, M1380 and T1382 with $Vpr_{mus}$ side chains of T79, R83,
184 R86 and E87 in Helix-3 result in the stabilisation of the sequence stretch that connect BP blades 6 and
185 7 ("C-terminal loop", Figs 2B and S3F). Moreover, side chain electrostatic interactions of $Vpr_{mus}$
186 residues R15, R75 and R76 with DCAF1 E1088, E1091 and E1093 lock the conformation of an "acidic
187 loop" upstream of BP blade 1, which is also unstructured and flexible in the absence of $Vpr_{mus}$ (Figs 2B,
188 C and S3D, F).
189 Notably, in previously determined structures of Vpx/DCAF1/SAMHD1 complexes the "acidic loop" is
190 a central point of ternary contact, providing a binding platform for positively charged amino acid side

191 chains in either the SAMHD1 N- or C-terminus [50-52]. For example, $Vpx_{sm}$ positions SAMHD1-CtD
192 in such a way, that SAMHD1 K622 engages in electrostatic interaction with the DCAF1 "acidic loop"
193 residue D1092 (Fig 2C, left panel). However, in the $Vpr_{mus}$ crystal structure the bound $Vpr_{mus}$ now blocks
194 access to the corresponding SAMHD1-CtD binding pocket, in particular by the positioning of an
195 extended N-terminal loop that precedes Helix-1. Additionally, $Vpr_{mus}$ side chains R15, R75 and R76
196 neutralise the DCAF1 "acidic loop", precluding the formation of further salt bridges to basic residues in
197 SAMHD1-CtD (Fig 2C, right panel).
198 To validate the importance of $Vpr_{mus}$ residues R15 and R75 for DCAF1-CtD-binding, charge reversal
199 mutations to glutamates were generated by site-directed mutagenesis. The circular dichroism (CD)
200 spectrum of the $Vpr_{mus}$ R15E R75E double mutant GST-fusion protein was identical to the wild type,
201 indicating similar secondary structure content and thus no major structural disturbances caused by the
202 amino acid substitutions (S3H Fig). The effect of the $Vpr_{mus}$ R15E R75E double mutant on complex
203 assembly was then analysed by GF chromatography. SDS-PAGE analysis of the resulting
204 chromatographic profile shows an almost complete loss of the DDB1/DCAF1-CtD/$Vpr_{mus}$/SAMHD1
205 complex peak (Fig 2D, fraction 6), when compared to the wild type, concomitant with enrichment of (i)
206 some proportion of $Vpr_{mus}$ R15E R75E-bound DDB1/DCAF1-CtD (Fig 2D, fraction 7), (ii) free
207 DDB1/DCAF1-CtD (fraction 7-8), and of (iii) $Vpr_{mus}$ R15E R75E/SAMHD1 binary complex (Fig 2D,
208 fraction 8-9). This suggests that charge reversal of $Vpr_{mus}$ side chains R15 and R75 weakens the strong
209 association with DCAF1 observed in wild type $Vpr_{mus}$, due to loss of electrostatic interaction with the
210 "acidic loop", in accordance with the crystal structure. Consequently, some proportion of Vpr-bound
211 SAMHD1 dissociates. This notion is further supported by GF analysis of binary combinations of the
212 $Vpr_{mus}$ R15E R75E double mutant with either SAMHD1 or DDB1/DCAF1-CtD. Incubation of $Vpr_{mus}$
213 R15E R75E with SAMHD1 followed by GF leads to co-elution of both proteins, concomitant with a
214 shift of the elution peak towards higher apparent molecular weight, compared to SAMHD1 alone (Fig.
215 2E, fractions 8-9). By contrast, incubation of the $Vpr_{mus}$ double mutant with DDB1/DCAF1-CtD does
216 not change the elution volume of the DDB/DCAF1-CtD species, and no band corresponding to Vpr can
217 be detected in the SDS-PAGE analysis of the corresponding fractions (Fig. 2F, fractions 7-8). These

218 data clearly demonstrate loss of interaction with DDB1/DCAF1-CtD upon charge reversal of $Vpr_{mus}$
219 residues 15 and 75, while the SAMHD1-binding activity is retained.
220

## 221 Cryo-EM analysis of CRL4-NEDD8$^{DCAF1-CtD}$/$Vpr_{mus}$/SAMHD1 conformational states and
## 222 dynamics

223 To obtain structural insight into $Vpr_{mus}$ in the context of a complete CRL4 assembly, and to understand
224 the SAMHD1 recruitment mechanism, we initiated cryo-EM analyses of the
225 CRL4$^{DCAF1-CtD}$/$Vpr_{mus}$/SAMHD1 assembly. In these studies, the small ubiquitin-like protein NEDD8
226 was enzymatically attached to the CUL4 subunit, in order to obtain its active form (S4A Fig) [55]. A
227 CRL4-NEDD8$^{DCAF1-CtD}$/$Vpr_{mus}$/SAMHD1 complex was reconstituted *in vitro* and purified by GF
228 chromatography (S4B Fig). 2D classification of the resulting particle images revealed considerable
229 compositional and conformational heterogeneity, especially regarding the presence and position of the
230 CUL4-NEDD8/ROC1 sub-complex (stalk) relative to DDB1/DCAF1/$Vpr_{mus}$ (core) (S4C Fig).
231 Two consecutive rounds of 3D classification yielded three particle populations, resulting in 3D
232 reconstructions at 8-10 Å resolution, which contained both the $Vpr_{mus}$-bound CRL4 core and the stalk
233 (conformational states-1, -2 and -3, Figs 3A and S4D-F). The quality of the 3D volumes was sufficient
234 to fit crystallographic models of core (Fig 2) and the stalk (PDB 2hye) [15] as rigid bodies (Figs 3B and
235 S4G). For the catalytic RING-domain subunit ROC1, only fragmented electron density was present near
236 the position it occupies in the crystallographic model (S4G Fig). In all three states, electron density was
237 selectively absent for the C-terminal CUL4 winged helix B (WHB) domain (residues 674-759), which
238 contains the NEDD8 modification site (K705), and for the preceding α-helix, which connects the CUL4
239 N-terminal domain to the WHB domain (S4G Fig). In accordance with this observation, the positions
240 of CRL5-attached NEDD8 and of the CRL4 ROC1 RING domain are sterically incompatible upon
241 superposition of their respective crystal structures (S4H Fig) [56].
242 Alignment of 3D volumes from states-1, -2 and -3 shows that core densities representing DDB1 BPA,
243 BPC, DCAF1-CtD and $Vpr_{mus}$ superimpose well, indicating that these components do not undergo major
244 conformational fluctuations and thus form a rigid platform for substrate binding and attachment of the
245 CRL4 stalk (Fig 3). However, rotation of DDB1 BPB around a hinge connecting it to BPC results in

246 three different orientations of state-1, -2 and -3 stalk regions relative to the core. BPB rotation angles
247 were measured as 69° between state-1 and -2, and 50° between state-2 and -3.
248 These data are in line with previous prediction based on extensive comparative crystal structure
249 analyses, which postulated an approx. 150° rotation of the CRL4 stalk around the core [13, 15, 16, 19,
250 57]. However, the left- and rightmost CUL4 orientations observed here, states-1 and -3 from our cryo-
251 EM analysis, indicate a slightly narrower stalk rotation range (119°), when compared to the outermost
252 stalk conformations modelled from previously determined crystal structures (143°) (Fig 3C). A possible
253 explanation for this discrepancy arises from inspection of the cryo-EM densities and fitted models,
254 revealing that along with the main interaction interface on DDB1 BPB there are additional molecular
255 contacts between CUL4 and DDB1. Specifically, in state-1, there is a contact between the loop
256 connecting helices D and E of CUL4 cullin repeat (CR)1 (residues 161-169) and a loop protruding from
257 BP blade 3 of DDB1 BPC (residues 795-801, S4I Fig). In state-3, the loop between CUL4 CR2 helices
258 D and E (residues 275-282) abuts a region in the C-terminal helical domain of DDB1 (residues 1110-
259 1127, S4J Fig). These auxiliary interactions might be required to lock the outermost stalk positions
260 observed here in order to confine the rotation range of CUL4.
261

262 **Molecular mechanism of SAMHD1-targeting**

263 A reanalysis of the cryo-EM data involving template-based particle picking and extensive 3D
264 classification allowed for separation of an additional homogeneous particle population (S5A, B Fig).
265 This subset of particle images yielded a 3D reconstruction at a nominal resolution of 7.3 Å that only
266 contained electron density corresponding to the CRL4 core (S5A-D Fig). Molecular models of DDB1
267 BP domains A and C (BPA, BPC), DCAF1-CtD and $Vpr_{mus}$, derived from our crystal structure (Fig 2),
268 could be fitted as rigid bodies into this cryo-EM volume (Fig 4A). No obvious electron density was
269 visible for the bulk of SAMHD1. However, close inspection revealed an additional tubular, slightly
270 arcing density feature, approx. 35 Å in length, located on the upper surface of the $Vpr_{mus}$ helix bundle,
271 approximately 17 Å away from and opposite of the $Vpr_{mus}$/DCAF1-CtD binding interface (Fig 4A, red
272 arrows). One end of the tubular volume contacts the middle of $Vpr_{mus}$ Helix-1, and the other end forms
273 additional contacts to the C-terminus of Helix-2 and the N-terminus of Helix-3 (Fig 4B). A local

274 resolution of 7.5-8 Å (S5C Fig) precluded the fitting of an atomic model. Considering the biochemical
275 data, showing that SAMHD1-CtD is sufficient for recruitment to DDB1/DCAF1/$Vpr_{mus}$, we hypothesise
276 that this observed electron density feature corresponds to a region of SAMHD1-CtD which physically
277 interacts with $Vpr_{mus}$. Given its dimensions, the putative SAMHD1-CtD density could accommodate
278 approx. 10 amino acid residues in a fully extended conformation or up to 23 residues in a kinked helical
279 arrangement. All previous crystal structure analyses [46], as well as secondary structure predictions
280 indicate that SAMHD1 residues C-terminal to the catalytic HD domain and C-terminal lobe (amino
281 acids 599-626) are disordered in the absence of additional binding partners. Accordingly, the N-terminal
282 globular domains of the SAMHD1 molecule might be flexibly linked to the C-terminal tether identified
283 here. In that case, the bulk of SAMHD1 samples a multitude of positions relative to the DDB1/DCAF1-
284 CtD/$Vpr_{mus}$ core, and consequently is averaged out in the process of cryo-EM reconstruction.
285 To test this hypothesis, $Vpr_{mus}$ amino acid residues in close proximity to the putative SAMHD1-CtD
286 density were substituted by site-directed mutagenesis. Specifically, $Vpr_{mus}$ W29 was changed to alanine
287 to block a hydrophobic contact with SAMHD1-CtD involving the aromatic side chain, and $Vpr_{mus}$ A66
288 was changed to a bulky tryptophan, in order to introduce a steric clash with SAMHD1-CtD (Fig 4B).
289 The structural integrity of the $Vpr_{mus}$ W29A A66W double mutant was confirmed by CD spectroscopy
290 (S3H Fig), and it was then assessed for complex formation with DDB1/DCAF1-CtD and SAMHD1 by
291 analytical GF. In comparison to wild type $Vpr_{mus}$, the W29A A66W mutant showed reduced
292 DDB1/DCAF1-CtD/$Vpr_{mus}$/SAMHD1 complex peak intensity (Fig 4C, fraction 6), concomitant with (i)
293 enrichment of DDB1/DCAF1-CtD/$Vpr_{mus}$ ternary complex, sub-stoichiometrically bound to SAMHD1
294 (Fig 4C, fraction 7), (ii) excess DDB1/DCAF1-CtD complex (Fig 4C, fraction 8), and (iii) excess
295 SAMHD1 (Fig 4C, fractions 9-10). In addition, binary combinations of the $Vpr_{mus}$ W29A A66W double
296 mutant with DDB1/DCAF1-CtD or SAMHD1 were also analysed by GF. These data show loss of
297 SAMHD1 interaction (Fig 4D), while the ability to bind DDB1/DCAF1-CtD is retained (Fig 4E).
298 Together, these biochemical analyses support a location of the SAMHD1-CtD binding site on the upper
299 surface of the $Vpr_{mus}$ helix bundle, as suggested by medium-resolution cryo-EM reconstruction.
300 To obtain additional experimental evidence, the $CRL4^{DCAF1\text{-}CtD}$/$Vpr_{mus}$/SAMHD1 assembly was further
301 examined by cross-linking mass spectrometry (CLMS), using the photo-reactive cross-linker sulfo-

302 SDA. This bi-functional compound contains an NHS-ester functional group on one end that reacts with
303 primary amines and hydroxyl groups, while the other end covalently links to any amino acid sidechain
304 within reach upon UV-activation via a carbene intermediate [58]. Accordingly, incubation of proteins
305 or protein complexes with sulfo-SDA, followed by UV-illumination, allows for high-density cross-
306 linking of lysine, and to a lesser extent serine, threonine and tyrosine side chains to amino acids within
307 reach of the SDA spacer group, with faster kinetics than pure NHS ester-based cross-linkers, due to the
308 short half-life of the UV-activated intermediate. Cross-linked peptides are subsequently identified by
309 mass spectrometry, and provide insights into the topology and residue-residue distances of proteins and
310 complexes [59]. In the case of the $CRL4^{DCAF1\text{-}CtD}/Vpr_{mus}$/SAMHD1 assembly, the majority of identified
311 cross-links that can be mapped onto the structure (468/519, 90.2%) are within the 25 Å violation
312 threshold imposed by the geometry of the SDA spacer. Interestingly, 8 of the 11 cross-links between
313 DDB1 and CUL4 are satisfied by the state-1 model, but increasingly violated in states-2 and -3 (S5E
314 Fig), supporting in solution the rotational flexibility of the CRL4 stalk with respect to DDB1/DCAF1-
315 CtD, as observed in cryo-EM (Fig 3).
316 An additional 300 cross-links involved SAMHD1, extending to the C-terminal half of CUL4, to a DDB1
317 sequence stretch comprising amino acid residues 900-1000, to parts of DCAF1-CtD and to $Vpr_{mus}$ (Figs
318 5A, S5E). The $CRL4^{DCAF1\text{-}CtD}/Vpr_{mus}$ residues exhibiting cross-links to SAMHD1 were mapped onto the
319 state-2 model, and showed the presence of a large, yet defined, interaction surface (Fig 5B). Importantly,
320 cross-links were apparent between the C-terminus of SAMHD1-CtD (residues K622, K626) and a region
321 in $Vpr_{mus}$ Helix-1 (residues 27-36), which forms a part of the putative SAMHD1-CtD binding interface
322 observed in cryo-EM, and which contains $Vpr_{mus}$ W29, one of the residues substituted in the mutagenesis
323 and biochemical analysis presented above (Fig 5B, purple spheres). In addition, amino acid residues
324 from the N-terminal portion of SAMHD1-CtD (residues K595, K596, T602-S606) cross-linked close to
325 the DCAF1-CtD "acidic loop" (residues 1092-1096), which is immobilised by Vpr near the proposed
326 SAMHD1-CtD binding site, and to the very C-terminus of CUL4 (residues Y744, A759), which is also
327 adjacent to the predicted SAMHD1-CtD binding position (Fig. 5B, pink spheres). Lastly, cross-links in
328 the SAMHD1 N-terminal SAM and catalytic HD domains almost exclusively involved patches of the
329 $CRL4^{DCAF1\text{-}CtD}/Vpr_{mus}$ surface surrounding and facing towards the putative SAMHD1-CtD attachment

330 point (Fig. 5B, light brown spheres). These observations are compatible with recruitment of SAMHD-
331 CtD on the upper surface of the Vpr helix bundle, as indicated by cryo-EM. In addition, the spatial
332 distribution of cross-links involving the SAMHD1 N-terminal domains suggest that these are flexibly
333 connected to SAMHD1-CtD, leading to highly variable positioning relative to $CRL4^{DCAF1\text{-}CtD}/Vpr_{mus}$ and
334 thus offering a multitude of cross-linking opportunities to nearby CRL4 components, again in line with
335 the cryo-EM reconstruction results, especially upon consideration of the positional heterogeneity of the
336 CUL4 stalk (Fig. 3).
337 In order to evaluate the distance information inherent in SAMHD1-CtD cross-links in a more
338 quantitative way, the volume accessible to SAMHD1-CtD for interaction with $CRL4^{DCAF1\text{-}CtD}/Vpr_{mus}$,
339 consistent with the CLMS distance restraints, was simulated using the DisVis software tool [60, 61].
340 For this analysis, SAMHD1-CtD was modelled as peptide in extended conformation. During the
341 simulation, the state-2 $CRL4^{DCAF1\text{-}CtD}/Vpr_{mus}$ molecular model was kept fixed, and a six-dimensional
342 search of all possible degrees of freedom of rotation and translation for the SAMHD1-CtD model in
343 molecular contact with $CRL4^{DCAF1\text{-}CtD}/Vpr_{mus}$ was computed and ranked according to agreement with
344 CLMS distance restraints. To visualise the output, all possible spatial positions of the centre of mass of
345 SAMHD1-CtD, which satisfy >50% of the CLMS restraints, were plotted as density map on the structure
346 of DCAF1-CtD/$Vpr_{mus}$ (Fig 5C). In accordance with the cryo-EM reconstruction, this independent
347 computational analysis also locates SAMHD1-CtD on top of the $Vpr_{mus}$ helix bundle.
348 Taken together, the structural, biochemical and CLMS data are consistent with a model where the very
349 C-terminus of SAMHD1 is recruited by $Vpr_{mus}$, to place the remaining SAMHD1 domains appropriately
350 for access to the catalytic machinery at the distal end of the CRL4 stalk.
351 These data allow for structural comparison with *neo*-substrate binding modes of Vpx and Vpr proteins
352 from different retrovirus lineages (Fig 6A-D). $Vpx_{HIV\text{-}2}$ and $Vpx_{sm}$ position SAMHD1-CtD at the side of
353 the DCAF1 BP domain through interactions with the N-termini of Vpx Helices-1 and -3 (Fig 6B) [50].
354 $Vpx_{mnd2}$ and $Vpx_{rcm}$ bind SAMHD1-NtD using a bipartite interface comprising the side of the DCAF1
355 BP and the upper surface of the Vpx helix bundle (Fig 6C) [51, 52]. $Vpr_{HIV\text{-}1}$ engages its ubiquitylation
356 substrate UNG2 using both the top and the upper edge of the $Vpr_{HIV\text{-}1}$ helix bundle (Fig 6D) [54]. Of
357 note, these upper-surface interaction interfaces only partially overlap with the $Vpr_{mus}$/SAMHD1-CtD

358 binding interface identified here and employ fundamentally different sets of interacting amino acid
359 residues. Thus, it appears that the molecular interaction interfaces driving Vpx/Vpr-mediated *neo*-
360 substrate recognition and degradation are not conserved between related SIV and HIV Vpx/Vpr
361 accessory proteins, even in cases where identical SAMHD1-CtD regions are targeted for recruitment.
362

363 # Discussion

364 Our X-ray crystallographic studies of the DDB1/DCAF1-CtD/$Vpr_{mus}$ assembly provide the first
365 structural insight into a class of "hybrid" SIV Vpr proteins. These are present in the $SIV_{agm}$ and
366 $SIV_{mus/deb/syk}$ lineages of lentiviruses and combine characteristics of related $Vpr_{HIV-1}$ and SIV Vpx
367 accessory proteins.
368 Like SIV Vpx, "hybrid" Vpr proteins down-regulate the host restriction factor SAMHD1 by recruiting
369 it to $CRL4^{DCAF1}$ for ubiquitylation and subsequent proteasomal degradation. However, using a
370 combination of X-ray, cryo-EM and CLMS analyses, we show that the molecular strategy, which $Vpr_{mus}$
371 evolved to target SAMHD1, is strikingly different from Vpx-containing SIV strains. In the two clades
372 of Vpx proteins, divergent amino acid sequence stretches just upstream of Helix-1 (variable region
373 (VR)1, S6A Fig), together with polymorphisms in the SAMHD1-N-terminus of the respective host
374 species, determine if HIV-2-type or $SIV_{mnd}$-type Vpx recognise SAMHD1-CtD or SAMHD1-NtD,
375 respectively. These recognition mechanisms result in positioning of SAMHD1-CtD or -NtD on the side
376 of the DCAF1 BP domain in a way that allows for additional contacts between SAMHD1 and DCAF1,
377 thus forming ternary Vpx/SAMHD1/DCAF1 assemblies with very low dissociation rates [50-52, 62].
378 In $Vpr_{mus}$, different principles determine the specificity for SAMHD1-CtD. Here, VR1 is not involved
379 in SAMHD1-CtD-binding at all, but forms additional interactions with DCAF1, which are not observed
380 in Vpx/DCAF1 protein complexes (S6A Fig). Molecular contacts between $Vpr_{mus}$ and SAMHD1 are
381 dispersed on Helices-1 and -3, facing away from the DCAF1 interaction site and immobilising
382 SAMHD1-CtD on the top side of the $Vpr_{mus}$ helix bundle (S6A Fig). Placement of SAMHD1-CtD in
383 such a position precludes stabilising ternary interaction with DCAF1-CtD, but still results in robust
384 SAMHD1 ubiquitylation *in vitro* and SAMHD1 degradation in cell-based assays [24].

385 The catalytic dNTPase activity of SAMHD1 depends on nucleotide-dependent oligomerisation,
386 mediated by two allosteric nucleotide-binding sites, where guanine-based nucleotides in the first site
387 induce dimer formation, and dNTP-binding to the second site leads to assembly of the catalytically
388 active tetramer. SAMHD1-CtD is essential for tetramer formation by contributing critical molecular
389 contacts to neighbouring protomers. Furthermore, tetramer destabilisation by CDK1/2-cyclinA-
390 dependent phosphorylation of T592 in SAMHD1-CtD endogenously attenuates SAMHD1 activity in
391 cycling cells [46, 63-65]. Accordingly, it is conceivable that by sequestering SAMHD1-CtD, $Vpr_{mus}$
392 destabilises the SAMHD1 tetramer, and in this way abrogates SAMHD1 activity, prior to inducing its
393 proteasomal degradation, in accordance with previous observation of $Vpx_{HIV-2}$-mediated SAMHD1
394 tetramer disassembly and inhibition of dNTPase activity [62].
395 Predictions regarding the molecular mechanism of SAMHD1-binding by other "hybrid" Vpr
396 orthologues are difficult due to sequence divergence. Even in $Vpr_{deb}$, the closest relative to $Vpr_{mus}$, only
397 approximately 50% of amino acid side chains lining the putative SAMHD1-CtD binding pocket are
398 conserved (S6A Fig). Previous *in vitro* ubiquitylation and cell-based degradation experiments did not
399 show a clear preference of $Vpr_{deb}$ for recruitment of either SAMHD1-NtD or –CtD [24, 49].
400 Furthermore, it is disputed if $Vpr_{deb}$ actually binds DCAF1 [66], which might possibly be explained by
401 amino acid variations in the very N-terminus and/or in Helix-3 (S6A Fig). $Vpr_{syk}$ is specific for
402 SAMHD1-CtD [49], but the majority of residues forming the binding platform for SAMHD1-CtD
403 observed in the present study are not conserved. The $SIV_{agm}$ lineage of Vpr proteins is even more
404 divergent, with significant differences not only in possible SAMHD1-contacting residues, but also in
405 the sequence stretches preceding Helix-1, and connecting Helices-2 and -3, as well as in the N-terminal
406 half of Helix-3 (S6A Fig). Furthermore, there are indications that recruitment of SAMHD1 by the
407 $Vpr_{agm.GRI}$ sub-type involves molecular recognition of both SAMHD1-NtD and –CtD [49, 53]. In
408 conclusion, recurring rounds of evolutionary lentiviral adaptation to the host SAMHD1 restriction
409 factor, followed by host re-adaptation, resulted in highly species-specific, diverse molecular modes of
410 Vpr-SAMHD1 interaction. Similar molecular arms races between cell-intrinsic antiviral host factors and
411 viral antagonists shaped the species-specific lentiviral antagonism of e.g. host restriction factors of the
412 APOBEC3 family and tetherin, through induction of their degradation by the respective viral antagonists

413 Vif or Nef/Vpu [67-69]. Furthermore, viral re-adaptation to certain simian and human variants of these
414 restriction factors, following cross-species transmission, took part in the emergence of pandemic HIV
415 strains, thus highlighting the importance of structural insight into these processes [9]. In addition to the
416 instance presented here, further structural characterisation of SAMHD1-Vpr complexes will be
417 necessary to fully define outcomes of this particular virus-host molecular arms race.
418 Previous structural investigation of DDB1/DCAF1/$Vpr_{HIV-1}$ in complex with the *neo*-substrate UNG2
419 demonstrated that $Vpr_{HIV-1}$ engages UNG2 by mimicking the DNA phosphate backbone. More precisely,
420 UNG2 residues, which project into the major groove of its endogenous DNA substrate, insert into a
421 hydrophobic cleft formed by $Vpr_{HIV-1}$ Helices-1, -2 and the N-terminal half of Helix-3 [54]. This
422 mechanism might rationalise $Vpr_{HIV-1}$'s extraordinary binding promiscuity, since the list of potential
423 $Vpr_{HIV-1}$ degradation substrates is significantly enriched in DNA- and RNA-binding proteins [27].
424 Moreover, promiscuous $Vpr_{HIV-1}$-induced degradation of host factors with DNA- or RNA-binding
425 activity has been proposed to induce cell cycle arrest at the G2/M phase border, which is the most
426 thoroughly described phenotype of Vpr proteins so far [26, 27, 70]. In $Vpr_{mus}$, the N-terminal half of
427 Helix-1 as well as the bulky amino acid residue W48, which is also conserved in $Vpr_{agm}$ and Vpx,
428 constrict the hydrophobic cleft (S6A, B Fig). Furthermore, the extended N-terminus of $Vpr_{mus}$ Helix-3
429 is not compatible with UNG2-binding due to steric exclusion (S6C Fig). In accordance with these
430 observations, $Vpr_{mus}$ does not down-regulate UNG2 in a human T cell line [27]. However, $Vpr_{mus}$, $Vpr_{syk}$
431 and $Vpr_{agm}$ also cause G2/M cell cycle arrest in their respective host cells [66, 71, 72]. This strongly
432 hints at the existence of further structural determinants in $Vpr_{mus}$, $Vpr_{syk}$, $Vpr_{agm}$ and potentially $Vpr_{HIV-1}$,
433 which regulate recruitment and ubiquitylation of DNA/RNA-binding host factors, in addition to the
434 hydrophobic, DNA-mimicking cleft on top of the three-helix bundle. Future efforts to structurally
435 characterise these determinants will further extend our understanding of how the Vpx/Vpr helical
436 scaffold binds, and in this way adapts to a multitude of *neo*-substrate epitopes.
437 Our cryo-EM reconstructions of $CRL4^{DCAF1-CtD}$/$Vpr_{mus}$/SAMHD1, complemented by CLMS, also
438 provide insights into the structural dynamics of CRL4 assemblies prior to ubiquitin transfer. The data
439 confirm previously described rotational movement of the CRL4 stalk, in the absence of constraints
440 imposed by a crystal lattice, creating a ubiquitylation zone around the $Vpr_{mus}$-modified substrate receptor

441 (Figs 3 and 7A) [13, 15, 16, 19, 57]. Missing density for the neddylated CUL4 WHB domain and for
442 the catalytic ROC1 RING domain indicates that these distal stalk elements are highly mobile and likely
443 sample a multitude of orientations relative to the CUL4 scaffold (Fig 7B). These observations are in line
444 with structure analyses of CRL1 and CRL5, where CUL1/5 neddylation leads to re-orientation of the
445 cullin WHB domain, and to release of the ROC1 RING domain from the cullin scaffold, concomitant
446 with stimulation of ubiquitylation activity [56]. Moreover, recent cryo-EM structure analysis of
447 $CRL1^{\beta\text{-}TRCP}$/IκBα demonstrated substantial mobility of pre-catalytic CUL1-NEDD8 WHB and ROC1
448 RING domains [73]. Such flexibility seems necessary to structurally organise multiple CRL1-dependent
449 processes, in particular the nucleation of a catalytic assembly, involving intricate protein-protein
450 interactions between NEDD8, CUL1, ubiquitin-charged E2 and substrate receptor. This synergistic
451 assembly then steers the ubiquitin C-terminus towards a substrate lysine for priming with ubiquitin [73].
452 Accordingly, our cryo-EM studies might indicate that similar principles apply for CRL4-catalysed
453 ubiquitylation. However, to unravel the catalytic architecture of CRL4, sophisticated cross-linking
454 procedures as in reference (73) will have to be pursued.
455 Intrinsic mobility of CRL4 stalk elements might assist the accommodation of a variety of sizes and
456 shapes of substrates in the CRL4 ubiquitylation zone and might rationalise the wide substrate range
457 accessible to CRL4 ubiquitylation through multiple DCAF receptors. Owing to selective pressure to
458 counteract the host's SAMHD1 restriction, HIV-2 and certain SIVs, amongst other viruses, have taken
459 advantage of this dynamic CRL4 architecture by modification of the DCAF1 substrate receptor with
460 Vpx/Vpr-family accessory proteins. By tethering either SAMHD1-CtD or -NtD to DCAF1, and in this
461 way flexibly recruiting the bulk of SAMHD1, the accessibility of lysine side chains both tether-proximal
462 and on the SAMHD1 globular domains to the CRL4 catalytic assembly might be further improved (Fig
463 7C, D). This ensures efficient Vpx/Vpr-mediated SAMHD1 priming, poly-ubiquitylation and
464 proteasomal degradation to stimulate virus replication. In addition, structural insight into this
465 evolutionary optimised, highly specific protein degradation machinery might inform the positioning of
466 novel $CRL4^{DCAF1}$-based synthetic modalities for targeted protein degradation, e.g. in the form of
467 proteolysis-targeting chimera-(PROTAC-) or molecular glue-type compounds [74, 75].

468 Lastly, while current highly active antiretroviral therapy (HAART) regimens are able to control HIV-1
469 replication in infected patients [76], they cannot eradicate the virus due to viral rebound after treatment
470 cessation, and they lead to emergence of resistant virus variants [77]. Accordingly, identification and
471 inhibition of novel targets, in addition to those already covered by HAART, are of high interest. In this
472 context, HIV accessory proteins have for a long time been regarded as promising drug targets [78, 79].
473 For example, preclinical research aiming at inhibition of Vif-mediated APOBEC3 degradation
474 culminated in the isolation of several compounds which impede HIV-1 replication [80-82]. Due to its
475 promiscuous host interactions, $Vpr_{HIV-1}$ is also considered an attractive antiretroviral target [83]. The
476 comparative structural analyses of Vpr/DCAF1-CtD interaction presented here might inform future
477 efforts to disrupt this interaction interface with small molecules, in order to abolish all Vpr-induced host
478 protein degradation processes at once, to maximise the inhibitory effect on virus replication.
479

480 # Methods

481 ## Protein expression and purification

482 Constructs were PCR-amplified from cDNA templates and inserted into the indicated expression
483 plasmids using standard restriction enzyme methods (S2 Table). pAcGHLT-B-DDB1 (plasmid #48638)
484 and pET28-UBA1 (plasmid #32534) were obtained from Addgene. The pOPC-UBA3-GST-APPBP1
485 co-expression plasmid, and the pGex6P2-UBC12 plasmid were obtained from MRC-PPU Reagents and
486 Services (clones 32498, 3879). Bovine erythrocyte ubiquitin and recombinant hsNEDD8 were
487 purchased from Sigma-Aldrich (U6253) and BostonBiochem (UL-812) respectively. Point mutations
488 were introduced by site-directed mutagenesis using KOD polymerase (Novagen). All constructs and
489 variants are summarised S3 Table.
490 Proteins expressed from vectors pAcGHLT-B, pGex6P1/2, pOPC and pET49b contained an N-terminal
491 GST-His-tag; pHisSUMO – N-terminal His-SUMO-tag; pET28, pRSF-Duet-1 – N-terminal His-tag;
492 pTri-Ex-6 – C-terminal His-tag. Constructs in vectors pAcGHLT-B and pTri-Ex-6 were expressed in
493 Sf9 cells, and constructs in vectors pET28, pET49b, pGex6P1/2, pRSF-Duet-1, and pHisSUMO in *E.*
494 *coli* Rosetta 2(DE3).

495 Recombinant baculoviruses (*Autographa californica nucleopolyhedrovirus* clone C6) were generated
496 as described previously [84]. Sf9 cells were cultured in Insect-XPRESS medium (Lonza) at 28°C in an
497 Innova 42R incubator shaker (New Brunswick) at a shaking speed of 180 rpm. In a typical preparation,
498 1 L of Sf9 cells at $3\times10^6$ cells/mL were co-infected with 4 mL of high titre DDB1 virus and 4 mL of
499 high titre DCAF1-CtD virus for 72 h.
500 For a typical *E. coli* Rosetta 2 (DE3) expression, 2 L of LB medium was inoculated with 20 mL of an
501 overnight culture and grown in a Multitron HT incubator shaker (Infors) at 37°C, 150 rpm until $OD_{600}$
502 reached 0.7. At that point, temperature was reduced to 18°C, protein expression was induced by addition
503 of 0.2 mM IPTG, and cultures were grown for further 20 h. During co-expression of CUL4 and ROC1
504 from pRSF-Duet, 50 µM zinc sulfate was added to the growth medium before induction.
505 Sf9 cells were pelleted by centrifugation at 1000 rpm, 4°C for 30 min using a JLA 9.1000 centrifuge
506 rotor (Beckman). *E. coli* cells were pelleted by centrifugation at 4000 rpm, 4°C for 15 min using the
507 same rotor. Cell pellets were resuspended in buffer containing 50 mM Tris, pH 7.8, 500 mM NaCl, 4
508 mM MgCl2, 0.5 mM tris-(2-carboxyethyl)-phosphine (TCEP), mini-complete protease inhibitors (1
509 tablet per 50 mL) and 20 mM imidazole (for His-tagged proteins only). 100 mL of lysis buffer was used
510 for resuspension of a pellet from 1 L Sf9 culture, and 35 mL lysis buffer per pellet from 1 L *E. coli*
511 culture. Before resuspension of CUL4/ROC1 co-expression pellets, the buffer pH was adjusted to 8.5.
512 5 µL Benzonase (Merck) was added and the cells lysed by passing the suspension at least twice through
513 a Microfluidiser (Microfluidics). Lysates were clarified by centrifugation at 48000xg for 45 min at 4°C.
514 Protein purification was performed at 4°C on an Äkta pure FPLC (GE) using XK 16/20 chromatography
515 columns (GE) containing 10 mL of the appropriate affinity resin. GST-tagged proteins were captured
516 on glutathione-Sepharose (GSH-Sepharose FF, GE), washed with 250 mL of wash buffer (50 mM Tris-
517 HCl pH 7.8, 500 mM NaCl, 4 mM $MgCl_2$, 0.5 mM TCEP), and eluted with the same buffer
518 supplemented with 20 mM reduced glutathione. His-tagged proteins were immobilised on Ni-Sepharose
519 HP (GE), washed with 250 mL of wash buffer supplemented with 20 mM imidazole, and eluted with
520 wash buffer containing 0.3 M imidazole. Eluent fractions were analysed by SDS-PAGE, and appropriate
521 fractions were pooled and reduced to 5 mL using centrifugal filter devices (Vivaspin). If applicable, 100
522 µg GST-3C protease, or 50 µg thrombin, per mg total protein, was added and the sample was incubated

523 for 12 h on ice to cleave off affinity tags. As second purification step, gel filtration chromatography
524 (GF) was performed on an Äkta prime plus FPLC (GE), with Superdex 200 16/600 columns (GE),
525 equilibrated in 10 mM Tris-HCl pH 7.8, 150 mM NaCl, 4 mM $MgCl_2$, 0.5 mM TCEP buffer, at a flow
526 rate of 1 mL/min. For purification of the CUL4/ROC1 complex, the pH of all purification buffers was
527 adjusted to 8.5. Peak fractions were analysed by SDS-PAGE, appropriate fractions were pooled and
528 concentrated to approx. 20 mg/mL, flash-frozen in liquid nitrogen in small aliquots and stored at -80°C.
529 Protein concentrations were determined with a NanoDrop spectrophotometer (ND 1000, Peqlab), using
530 theoretical absorption coefficients calculated based upon the amino acid sequence by ProtParam on the
531 ExPASy webserver [85].
532

533 **Analytical gel filtration analysis**

534 Prior to gel filtration analysis affinity tags were removed by incubation of 30 µg GST-3C protease with
535 6 µM of each protein component in a volume of 150 µL wash buffer, followed by incubation on ice for
536 12 h. In order to remove the cleaved GST-tag and GST-3C protease, 20 µL GSH-Sepharose FF beads
537 (GE) were added and the sample was rotated at 4 °C for one hour. GSH-Sepharose beads were removed
538 by centrifugation at 4°C, 3500 rpm for 5 min, and 120 µL of the supernatant was loaded on an analytical
539 GF column (Superdex 200 10/300 GL, GE), equilibrated in 10 mM Tris-HCl pH 7.8, 150 mM NaCl,
540 4 mM $MgCl_2$, 0.5 mM TCEP, at a flow rate of 0.5 mL/min. 1 mL fractions were collected and analysed
541 by SDS-PAGE. For the following control samples, 120 µl of purified protein was applied directly to the
542 GF column, because no purification tag had to be removed by cleavage: SAMHD1, T4L-SAMHD1-
543 CtD, SAMHD1-ΔCtD. For these samples, the concentration was adjusted to 18 µM, 37 µM and 30 µM,
544 respectively, to account for the lower extinction coefficient of these isolated protein components, in
545 order to allow for better visualisation of the elution peak. The GF column was calibrated using the high
546 molecular weight range (HMW) Gel Filtration Calibration Kit (GE) according to the manufacturer's
547 instructions.
548

549 ***In vitro* ubiquitylation assays**

550 160 µL reactions were prepared, containing 0.5 µM substrate (indicated SAMHD1 constructs, S2 Fig),
551 0.125 µM DDB1/DCAF1-CtD, 0.125 µM CUL4/ROC1, 0.125 µM HisSUMO-T4L-$Vpr_{mus}$ (residues 1-
552 92), 0.25 µM UBCH5C, 15 µM ubiquitin in 20 mM Tris-HCl pH 7.8, 150 mM NaCl, 2.5 mM $MgCl_2$,
553 2.5 mM ATP. In control reactions, certain components were left out as indicated in S2 Fig. A 30 µl
554 sample for SDS-PAGE analysis was taken (t=0). Reactions were initiated by addition of 0.05 µM UBA1,
555 incubated at 37°C, and 30 µl SDS-PAGE samples were taken after 1 min, 2 min, 5 min and 15 min,
556 immediately mixed with 10 µl 4x SDS sample buffer and boiled at 95°C for 5 min. Samples were
557 analysed by SDS-PAGE.
558

559 ***In vitro* neddylation of CUL4/ROC1**

560 For initial neddylation tests, a 200 µL reaction was prepared, containing 8 µM CUL4/ROC1, 1.8 µM
561 UBC12, 30 µM NEDD8 in 50 mM Tris-HCl pH 7.8, 150 mM NaCl, 2.5 mM $MgCl_2$, 2.5 mM ATP. 2x
562 30 µL samples were taken for SDS-PAGE, one was immediately mixed with 10 µL 4x SDS sample
563 buffer, the other one incubated for 60 min at 25°C. The reaction was initiated by addition of 0.7 µM
564 APPBP1/UBA3, incubated at 25°C, and 30 µL SDS-PAGE samples were taken after 1 min, 5 min,
565 10 min, 30 min and 60 min, immediately mixed with 10 µL 4x SDS sample buffer and boiled at 95°C
566 for 5 min. Samples were analysed by SDS-PAGE. Based on this test, the reaction was scaled up to 1 mL
567 and incubated for 5 min at 25°C. Reaction was quenched by addition of 5 mM TCEP and immediately
568 loaded onto a Superdex 200 16/600 GF column (GE), equilibrated in 10 mM Tris-HCl pH 7.8, 150 mM
569 NaCl, 4 mM $MgCl_2$, 0.5 mM TCEP at a flow rate of 1 mL/min. Peak fractions were analysed by SDS-
570 PAGE, appropriate fractions were pooled and concentrated to ~20 mg/mL, flash-frozen in liquid
571 nitrogen in small aliquots and stored at -80°C.
572

573 **X-ray crystallography sample preparation, crystallisation, data collection and structure**
574 **solution**

575 **DDB1/DCAF1-CtD complex**. DDB1/DCAF1-CtD crystals were grown by the hanging drop vapour
576 diffusion method, by mixing equal volumes (1 µL) of DDB1/DCAF1-CtD solution at 10 mg/mL with
577 reservoir solution containing 100 mM Tri-Na citrate pH 5.5, 18% PEG 1000 and suspending over a 500

578 µl reservoir. Crystals grew over night at 18°C. Crystals were cryo-protected in reservoir solution
579 supplemented with 20% glycerol and cryo-cooled in liquid nitrogen. A data set from a single crystal was
580 collected at Diamond Light Source (Didcot, UK) at a wavelength of 0.92819 Å. Data were processed
581 using XDS [86] (S1 Table), and the structure was solved using molecular replacement with the program
582 MOLREP [87] and available structures of DDB1 (PDB 3e0c) and DCAF1-CtD (PDB 4cc9) [50] as
583 search models. Iterative cycles of model adjustment with the program Coot [88], followed by refinement
584 using the program PHENIX [89] yielded final $R/R_{free}$ factors of 22.0%/27.9% (S1 Table). In the model,
585 94.5 % of residues have backbone dihedral angles in the favoured region of the Ramachandran plot, the
586 remainder fall in the allowed regions, and none are outliers. Details of data collection and refinement
587 statistics are presented in S1 Table. Coordinates and structure factors have been deposited in the PDB,
588 accession number 6zue.

589 **DDB1/DCAF1-CtD/T4L-$Vpr_{mus}$ (1-92) complex**. The DDB1/DCAF1-CtD/$Vpr_{mus}$ complex was
590 assembled by incubation of purified DDB1/DCAF1-CtD and HisSUMO-T4L-$Vpr_{mus}$ (residues 1-92), at
591 a 1:1 molar ratio, in a buffer containing 50 mM Bis-tris propane pH 8.5, 0.5 M NaCl, 4 mM $MgCl_2$, 0.5
592 mM TCEP, containing 1 mg of HRV-3C protease for HisSUMO-tag removal. After incubation on ice
593 for 12 h, the sample was loaded onto a Superdex 200 16/600 GF column (GE), with a 1 mL GSH-
594 Sepharose FF column (GE) connected in line. The column was equilibrated with 10 mM Bis-tris propane
595 pH 8.5, 150 mM NaCl, 4 mM MgCl2, and 0.5 mM TCEP. The column flow rate was 1 mL/min. GF
596 fractions were analysed by SDS-PAGE, appropriate fractions were pooled and concentrated to 4.5
597 mg/mL.

598 Crystals were prepared by the sitting drop vapour diffusion method, by mixing equal volumes (200 nL)
599 of the protein complex at 4.5 mg/mL and reservoir solution containing 8-10% PEG 4000 (w/v), 200 mM
600 $MgCl_2$, 100 mM HEPES-NaOH, pH 7.0-8.2. The reservoir volume was 75 µL. Crystals grew after at
601 least 4 weeks of incubation at 4°C. Crystals were cryo-protected in reservoir solution supplemented with
602 20% glycerol and cryo-cooled in liquid nitrogen. Data sets from two single crystals were collected,
603 initially at BESSY II (Helmholtz-Zentrum Berlin, HZB) at a wavelength of 0.91841 Å, and later at
604 ESRF (Grenoble) at a wavelength of 1 Å. Data sets were processed separately using XDS [86] and
605 XDSAPP [90]. The structure was solved by molecular replacement, using the initial BESSY data set,

606 with the program PHASER [91], and the following structures as search models: DDB1/DCAF1-CtD
607 (this work) and T4L variant E11H (PDB 1qt6) [92]. After optimisation of the initial model and
608 refinement against the higher-resolution ESRF data set, $Vpr_{mus}$ was placed manually into the density,
609 using an NMR model of $Vpr_{HIV-1}$ (PDB 1m8l) [93] as guidance. Iterative cycles of model adjustment
610 with the program Coot [88], followed by refinement using the program PHENIX [89] yielded final
611 $R/R_{free}$ factors of 21.61%/26.05%. In the model, 95.1 % of residues have backbone dihedral angles in
612 the favoured region of the Ramachandran plot, the remainder fall in the allowed regions, and none are
613 outliers. Details of data collection and refinement statistics are presented in S1 Table. Coordinates and
614 structure factors have been deposited in the PDB, accession number 6zx9.
615

616 **Cryo-EM sample preparation and data collection**

617 **Complex assembly**. Purified CUL4-NEDD8/ROC1, DDB1/DCAF1-CtD, GST-$Vpr_{mus}$ and rhesus
618 macaque SAMHD1, 1 µM each, were incubated in a final volume of 1 mL of 10 mM Tris-HCl pH 7.8,
619 150 mM NaCl, 4 mM $MgCl_2$, 0.5 mM TCEP, supplemented with 1 mg of GST-3C protease. After
620 incubation on ice for 12 h, the sample was loaded onto a Superdex 200 16/600 GF column (GE),
621 equilibrated with the same buffer at 1 mL/min, with a 1 mL GSH-Sepharose FF column (GE) connected
622 in line. GF fractions were analysed by SDS-PAGE, appropriate fractions were pooled and concentrated
623 to 2.8 mg/mL.

624 **Grid preparation.** 3.5 µl protein solution containing 0.05 µM CUL4-NEDD8/ROC1/DDB1/DCAF1-
625 CtD/$Vpr_{mus}$/SAMHD1 complex and 0.25 µM UBCH5C-ubiquitin conjugate (S4 A, B Fig) were applied
626 to a 300 mesh Quantifoil R2/4 Cu/Rh holey carbon grid (Quantifoil Micro Tools GmbH) coated with an
627 additional thin carbon film as sample support and stained with 2% uranyl acetate for initial
628 characterisation. For cryo-EM, a fresh 400 mesh Quantifoil R1.2/1.3 Cu holey carbon grid (Quantifoil
629 Micro Tools GmbH) was glow-discharged for 30 s using a Harrick plasma cleaner with technical air at
630 0.3 mbar and 7 W. 3.5 µl protein solution containing 0.4 µM CUL4-NEDD8/ROC1/DDB1/DCAF1-
631 CtD/$Vpr_{mus}$/SAMHD1 complex and 2 µM UBCH5C-ubiquitin conjugate were applied to the grid,
632 incubated for 45 s, blotted with a Vitrobot Mark II device (FEI, Thermo Fisher Scientific) for 1-2 s at
633 8°C and 80% humidity, and plunged in liquid ethane. Grids were stored in liquid nitrogen until imaging.

634 **Cryo-EM data collection.** Initial negative stain and cryo-EM datasets were collected automatically
635 for sample quality control and low-resolution reconstructions on a 120 kV Tecnai Spirit cryo-EM (FEI,
636 Thermo Fisher Scientific) equipped with a F416 CMOS camera (TVIPS) using Leginon [94, 95].
637 Particle images were then analysed by 2D classification and initial model reconstruction using SPHIRE
638 [96], cisTEM [97] and Relion 3.07 [98]. These data revealed the presence of the complexes containing
639 both DDB1/DCAF1-CtD/$Vpr_{mus}$ (core) and CUL4/ROC1 (stalk). High-resolution data was collected on
640 a 300 kV Tecnai Polara cryo-EM (FEI, Thermo Fisher Scientific) equipped with a K2summit direct
641 electron detector (Gatan) at a nominal magnification of 31000x, with a pixel size of 0.625 Å/px on the
642 object scale. In total, 3644 movie stacks were collected in super-resolution mode using Leginon [94, 95]
643 with the following parameters: defocus range of 0.5-3.0 µm, 40 frames per movie, 10 s exposure time,
644 electron dose of 1.25 e/$Å^2$/s and a cumulative dose of 50 e/$Å^2$ per movie.
645

646 **Cryo-EM computational analysis**

647 Movies were aligned and dose-weighted using MotionCor2 [99] and initial estimation of the contrast
648 transfer function (CTF) was performed with the CTFFind4 package [100]. Resulting micrographs were
649 manually inspected to exclude images with substantial contaminants (typically large protein aggregates
650 or ice contaminations) or grid artefacts. Power spectra were manually inspected to exclude images with
651 astigmatic, weak, or poorly defined spectra. After these quality control steps the dataset included 2322
652 micrographs (63% of total). At this stage, the data set was picked twice and processed separately, to
653 yield reconstructions of states-1, -2 and -3 (analysis 1) and of the core (analysis 2).
654 For **analysis 1**, particle positions were determined using cisTEMs Gaussian picking routine, yielding
655 959,155 particle images in total. After two rounds of 2D-classification, 227,529 particle images were
656 selected for further processing (S4C, D Fig). Using this data, an initial model was created using Relion
657 3.07. The resulting map yielded strong signal for the core but only fragmented stalk density, indicating
658 a large heterogeneity in the stalk-region within the data set. This large degree of compositional (+/-
659 stalk) and conformational heterogeneity (movement of the stalk relative to the core) made the
660 classification challenging. Accordingly, alignment and classification were carried out simultaneously.
661 The first objective was to separate the data set into three categories: “junk”, “core” and “core+stalk”.

662 Therefore, the stalk was deleted from the initial model using the "Eraser"-tool in Chimera [101]. This
663 core-map was used as an initial model for the Tier 1 3D-classification with Relion 3.07 at a decimated
664 pixel size of 2.5 Å/px. The following parameters were used: number of classes K=6, T=10, global step
665 search=7.5°, number of iterations= 25. The classification yielded two classes containing the stalk
666 (classes 3 and 5 containing 23% and 22% of the particle images, respectively) (S4D Fig). These particles
667 were pooled and directed into Tier 2 3D-classification using the following parameters: number of classes
668 K=6, T=10, global step search=7.5°, number of iterations=25. Three of these classes yielded medium-
669 resolution maps with interpretable features (states-1, -2 and -3, S4D Fig). These three classes were
670 refined individually using 3D autorefinement in Relion 3.07, resulting in maps with resolution ranging
671 from 7.8 Å – 8.9 Å (S4E-G Fig).
672 For **analysis 2**, particle positions were determined using template matching with a filtered map
673 comprising core and stalk using the software Gautomatch (https://www2.mrc-
674 lmb.cam.ac.uk/research/locally-developed-software/zhang-software/). 712,485 particle images were
675 found, extracted with Relion 3.07 and subsequently 2D-classified using cryoSPARC [102], resulting in
676 505,342 particle images after selection (S5A, B Fig). These particle images were separated into two
677 equally sized subsets and Tier 1 3D-classification was performed using Relion 3.07 on both of them to
678 reduce computational burden (S5B Fig). The following parameters were used: initial model="core",
679 number of classes K=4, T=10, global step search=7.5°, number of iterations=25, pixel size 3.75 Å/px.
680 From these, the ones possessing both core and stalk were selected. Classes depicting a similar stalk
681 orientation relative to the core were pooled and directed into Tier 2 as three different subpopulations
682 containing 143,172, 193,059 and 167,666 particle images, respectively (S5B Fig).
683 For Tier 2, each subpopulation was classified separately into 4 classes each. From these 12 classes, all
684 particle images exhibiting well-defined densities for core and stalk were pooled and labelled
685 "core+stalk", resulting in 310,801 particle images in total. 193,096 particle images representing classes
686 containing only the core were pooled and labelled "core" (S5B Fig)
687 For Tier 3, the "core" particle subset was separated into 4 classes which yielded uninterpretable
688 reconstructions lacking medium- or high-resolution features. The "core+stalk" subset was separated into
689 6 classes, with 5 classes containing both stalk and core (S5B Fig) and one class consisting only of the

690 core with $Vpr_{mus}$ bound. The 5 classes with stalk showed similar stalk orientations as the ones obtained
691 from analysis 1 (see above, S4 Fig), but refined individually to lower resolution as in analysis 1 and
692 were discarded. However, individual refinement of the core-only tier 3 class yielded a 7.3 Å
693 reconstruction (S5C, D Fig).
694

695 **Molecular visualisation, rigid body fitting, 3D structural alignments, rotation and**
696 **interface analysis**

697 Density maps and atomic models were visualised using Coot [88], PyMOL (Schrödinger) and UCSF
698 Chimera [101]. Rigid body fits and structural alignments were performed using the program UCSF
699 Chimera [101]. Rotation angles between extreme DDB1 BPB domain positions were measured using
700 the DynDom server [103] (http://dyndom.cmp.uea.ac.uk/dyndom/runDyndom.jsp). Molecular
701 interfaces were analysed using the EBI PDBePISA server [104] (https://www.ebi.ac.uk/msd-
702 srv/prot_int/cgi-bin/piserver).
703

704 **Multiple sequence alignment**

705 A multiple sequence alignment was calculated using the EBI ClustalOmega server [105]
706 (https://www.ebi.ac.uk/Tools/msa/clustalo/), and adjusted manually using the program GeneDoc [106].
707

708 **Cross-linking mass spectrometry (CLMS)**

709 **Complex assembly.** Purified CUL4/ROC1, DDB1/DCAF1-CtD, GST-$Vpr_{mus}$ and rhesus macaque
710 SAMHD1, 1 µM each, were incubated in a volume of 3 mL buffer containing 10 mM HEPES pH 7.8,
711 150 mM NaCl, 4 mM $MgCl_2$, 0.5 mM TCEP, supplemented with 1 mg GST-3C protease. After
712 incubation on ice for 12 h, the sample was loaded onto a Superdex 200 16/600 GF column (GE),
713 equilibrated with the same buffer, at a flow rate of 1 mL/min with a 1 mL GSH-Sepharose FF column
714 (GE) connected in line. GF fractions were analysed by SDS-PAGE, appropriate fractions were pooled
715 and concentrated to 6 mg/mL.

716 **Photo-Crosslinking.** The cross-linker sulfo-SDA (sulfosuccinimidyl 4,4′-azipentanoate) (Thermo
717 Scientific) was dissolved in cross-linking buffer (10 mM HEPES pH 7.8, 150 mM NaCl, 4 mM

718 $MgCl_2$, 0.5 mM TCEP) to 100 mM before use. The labelling step was performed by incubating
719 18 µg aliquots of the complex at 1 mg/mL with 2, 1, 0.5, 0.25, 0.125 mM sulfo-SDA, added,
720 respectively, for an hour. The samples were then irradiated with UV light at 365 nm, to form cross-
721 links, for 20 min and quenched with 50 mM $NH_4HCO_3$ for 20 min. All steps were performed on
722 ice. Reaction products were separated on a Novex Bis-Tris 4–12% SDS−PAGE gel (Life
723 Technologies). The gel band corresponding to the cross-linked complex was excised and digested
724 with trypsin (Thermo Scientific Pierce) [107] and the resulting tryptic peptides were extracted and
725 desalted using C18 StageTips [108]. Eluted peptides were fractionated on a Superdex Peptide
726 3.2/300 increase column (GE Healthcare) at a flow rate of 10 µL/min using 30% (v/v) acetonitrile
727 and 0.1 % (v/v) trifluoroacetic acid as mobile phase. 50 µL fractions were collected and vacuum-
728 dried.

729 **CLMS acquisition.** Samples for analysis were resuspended in 0.1% (v/v) formic acid, 3.2% (v/v)
730 acetonitrile. LC-MS/MS analysis was performed on an Orbitrap Fusion Lumos Tribrid mass
731 spectrometer (Thermo Fisher) coupled on-line with an Ultimate 3000 RSLCnano HPLC system
732 (Dionex, Thermo Fisher). Samples were separated on a 50 cm EASY-Spray column (Thermo Fisher).
733 Mobile phase A consisted of 0.1% (v/v) formic acid and mobile phase B of 80% (v/v) acetonitrile with
734 0.1% (v/v) formic acid. Flow rates were 0.3 µL/min using gradients optimized for each chromatographic
735 fraction from offline fractionation, ranging from 2% mobile phase B to 55% mobile phase B over
736 90 min. MS data were acquired in data-dependent mode using the top-speed setting with a 3 s cycle
737 time. For every cycle, the full scan mass spectrum was recorded using the Orbitrap at a resolution of
738 120,000 in the range of 400 to 1,500 m/z. Ions with a precursor charge state between 3+ and 7+ were
739 isolated and fragmented. Analyte fragmentation was achieved by Higher-Energy Collisional
740 Dissociation (HCD) [109] and fragmentation spectra were then recorded in the Orbitrap with a resolution
741 of 50,000. Dynamic exclusion was enabled with single repeat count and 60 s exclusion duration.

742 **CLMS processing.** A recalibration of the precursor m/z was conducted based on high-confidence
743 (<1% false discovery rate (FDR)) linear peptide identifications. The re-calibrated peak lists were
744 searched against the sequences and the reversed sequences (as decoys) of cross-linked peptides using
745 the Xi software suite (v.1.7.5.1) for identification [110]. Final crosslink lists were compiled using the

746 identified candidates filtered to <1% FDR on link level with xiFDR v.2.0 [111] imposing a minimum
747 of 20% sequence coverage and 4 observed fragments per peptide.
748 **CLMS analysis.** In order to sample the accessible interaction volume of the SAMHD1-CtD consistent
749 with CLMS data, a model for SAMHD1 was generated using I-TASSER [112]. The SAMHD1-CtD,
750 which adopted a random coil configuration, was extracted from the model. In order to map all crosslinks,
751 missing loops in the complex structure were generated using MODELLER [113]. An interaction volume
752 search was then submitted to the DisVis webserver [61] with an allowed distance between 1.5 Å and 22
753 Å for each restraint using the "complete scanning" option. The rotational sampling interval was set to
754 9.72° and the grid voxel spacing to 1Å. The accessible interaction volume was visualised using UCSF
755 Chimera [101].
756
757 **Circular dichroism (CD) spectroscopy**
758 In order to evaluate the secondary structure content of GST-tagged $Vpr_{mus}$, and the double mutants
759 R15E/R75E and W29A/A66W, CD spectroscopy was performed. Protein samples were dialysed
760 overnight at 4°C against CD buffer (100 mM NaF, 10 mM $K_2HPO_4/KH_2PO_4$ mixture, pH 8.5), and
761 protein concentration then adjusted to 0.2 mg/ml. For each sample, three replicate CD spectra were
762 recorded in 1.0 nm steps over the range of 190-260 nm. Measurements were performed in 0.05 cm path-
763 length quartz cuvettes (Hellma, Mühlheim, Germany) at 20°C on a Chirascan spectropolarimeter
764 (Applied Photophysics, London, UK). A reference spectrum of CD buffer was subtracted from the
765 averaged protein sample spectrum. Measured ellipticity in millidegrees (m°) was converted to molar
766 ellipticity [Θ] according to equation Θ=m°*M/(10xLxC), where M is the average protein molecular
767 weight, L is path length of the measurement cell, and C is the molar protein concentration. Molar
768 ellipticity was plotted against wavelength using SigmaPlot version 14.0 (Systat Software Inc., San Jose,
769 California, USA).
770
771 **Acknowledgments**
772 We thank the MPI-MG for granting access to the TEM instruments of the microscopy and cryo-EM
773 service group. We thank Dr. Manfred Weiss and the scientific staff of the BESSY-MX (Macromolecular

774 X-ray Crystallography)/Helmholtz Zentrum Berlin für Materialien und Energie at beamlines BL14.1,
775 BL14.2, and BL14.3 operated by the Joint Berlin MX-Laboratory at the BESSY II electron storage ring
776 (Berlin-Adlershof, Germany) as well as the scientific staff of the ESRF (Grenoble, France) at beamlines
777 ID30A-3, ID30B, ID23-1, ID23-2, and ID29 for continuous support. We acknowledge Diamond Light
778 Source (Didcot, UK) for access and support of the synchrotron beamline I04 and cryo-EM facilities at
779 the UK's national Electron Bio-imaging Centre (eBIC). Furthermore, the authors acknowledge the
780 North-German Supercomputing Alliance (HLRN) and the HPC for Research cluster of the Berlin
781 Institute of Health for providing HPC resources. We are grateful to Prof. Udo Heinemann and Jianhui
782 Wang (Max-Delbrück-Centrum, Berlin, Germany) for access to and assistance during CD spectroscopy.
783 The pHisSUMO plasmid was a generous gift from Dr. Evangelos Christodoulou (The Francis Crick
784 Institute, London, UK). The rhesus macaque SAMHD1 cDNA template was a generous gift from Prof.
785 Michael Emerman (Fred Hutchinson Cancer Research Center, Seattle, USA). Recombinant
786 BAC10:1629KO bacmid was a generous gift from Prof. Ian Jones (University of Reading, UK).
787 pAcGHLT-B-DDB1 was a gift from Prof. Ning Zheng (Addgene plasmid 48638). pET28-mE1 was a
788 gift from Prof. Jorge Eduardo Azevedo (Addgene plasmid 32534).
789

790 **Data availability**

791 The coordinates and structure factors for the crystal structures have been deposited at the Protein Data
792 Bank (PDB) with the accession codes 6ZUE (DDB1/DCAF1-CtD) and 6ZX9 (DDB1/DCAF1-
793 CtD/T4L-$Vpr_{mus}$ 1-92). Cryo-EM reconstructions have been deposited at the Electron Microscopy Data
794 Bank (EMDB) with the accession codes EMD-10611 (core), EMD-10612 (conformational state-1),
795 EMD-10613 (state-2) and EMD-10614 (state-3). CLMS data have been deposited at the PRIDE database
796 [114] with the accession code PXD020453, reviewer password fCrQG2u8.

797 # References


798 1. Randow F, Lehner PJ. Viral avoidance and exploitation of the ubiquitin system. Nat Cell Biol.
799 2009;11(5):527-34. doi: 10.1038/ncb0509-527.
800 2. Isaacson MK, Ploegh HL. Ubiquitination, ubiquitin-like modifiers, and deubiquitination in viral
801 infection. Cell host & microbe. 2009;5(6):559-70. doi: 10.1016/j.chom.2009.05.012.
802 3. Gustin JK, Moses AV, Fruh K, Douglas JL. Viral takeover of the host ubiquitin system. Front
803 Microbiol. 2011;2:161. doi: 10.3389/fmicb.2011.00161.
804 4. Barry M, Fruh K. Viral modulators of cullin RING ubiquitin ligases: culling the host defense. Science's
805 STKE : signal transduction knowledge environment. 2006;2006(335):pe21. Epub 2006/05/18. doi:
806 10.1126/stke.3352006pe21.
807 5. Mahon C, Krogan NJ, Craik CS, Pick E. Cullin E3 ligases and their rewiring by viral factors.
808 Biomolecules. 2014;4(4):897-930. Epub 2014/10/15. doi: 10.3390/biom4040897.
809 6. Becker T, Le-Trilling VTK, Trilling M. Cellular Cullin RING Ubiquitin Ligases: Druggable Host
810 Dependency Factors of Cytomegaloviruses. Int J Mol Sci. 2019;20(7). doi: 10.3390/ijms20071636.
811 7. Seissler T, Marquet R, Paillart JC. Hijacking of the Ubiquitin/Proteasome Pathway by the HIV
812 Auxiliary Proteins. Viruses. 2017;9(11). doi: 10.3390/v9110322.
813 8. Zheng N, Shabek N. Ubiquitin Ligases: Structure, Function, and Regulation. Annu Rev Biochem.
814 2017;86:14.1-29.
815 9. Sauter D, Kirchhoff F. Key Viral Adaptations Preceding the AIDS Pandemic. Cell host & microbe.
816 2019;25(1):27-38. doi: 10.1016/j.chom.2018.12.002.
817 10. Sharp PM, Hahn BH. Origins of HIV and the AIDS pandemic. Cold Spring Harbor perspectives in
818 medicine. 2011;1(1):a006841. Epub 2012/01/10. doi: 10.1101/cshperspect.a006841.
819 11. Hatziioannou T, Del Prete GQ, Keele BF, Estes JD, McNatt MW, Bitzegeio J, et al. HIV-1-induced
820 AIDS in monkeys. Science. 2014;344(6190):1401-5. Epub 2014/06/21. doi: 10.1126/science.1250761.
821 12. Malim MH, Bieniasz PD. HIV Restriction Factors and Mechanisms of Evasion. Cold Spring Harbor
822 perspectives in medicine. 2012;2(5):a006940. Epub 2012/05/04. doi: 10.1101/cshperspect.a006940.
823 13. Fischer ES, Scrima A, Bohm K, Matsumoto S, Lingaraju GM, Faty M, et al. The molecular basis of
824 CRL4DDB2/CSA ubiquitin ligase architecture, targeting, and activation. Cell. 2011;147(5):1024-39. Epub
825 2011/11/29. doi: 10.1016/j.cell.2011.10.035.

826 14. Lee J, Zhou P. DCAFs, the missing link of the CUL4-DDB1 ubiquitin ligase. Molecular cell.
827 2007;26(6):775-80. Epub 2007/06/26. doi: 10.1016/j.molcel.2007.06.001.
828 15. Angers S, Li T, Yi X, MacCoss MJ, Moon RT, Zheng N. Molecular architecture and assembly of the
829 DDB1-CUL4A ubiquitin ligase machinery. Nature. 2006;443(7111):590-3. Epub 2006/09/12. doi:
830 10.1038/nature05175.
831 16. Scrima A, Konickova R, Czyzewski BK, Kawasaki Y, Jeffrey PD, Groisman R, et al. Structural basis of
832 UV DNA-damage recognition by the DDB1-DDB2 complex. Cell. 2008;135(7):1213-23. Epub 2008/12/27. doi:
833 10.1016/j.cell.2008.10.045.
834 17. Zimmerman ES, Schulman BA, Zheng N. Structural assembly of cullin-RING ubiquitin ligase
835 complexes. Current opinion in structural biology. 2010;20(6):714-21. Epub 2010/10/01. doi:
836 10.1016/j.sbi.2010.08.010.
837 18. Andrejeva J, Young DF, Goodbourn S, Randall RE. Degradation of STAT1 and STAT2 by the V
838 proteins of simian virus 5 and human parainfluenza virus type 2, respectively: consequences for virus replication
839 in the presence of alpha/beta and gamma interferons. Journal of virology. 2002;76(5):2159-67. doi:
840 10.1128/jvi.76.5.2159-2167.2002.
841 19. Li T, Chen X, Garbutt KC, Zhou P, Zheng N. Structure of DDB1 in complex with a paramyxovirus V
842 protein: viral hijack of a propeller cluster in ubiquitin ligase. Cell. 2006;124(1):105-17. Epub 2006/01/18. doi:
843 10.1016/j.cell.2005.10.033.
844 20. Trilling M, Le VT, Fiedler M, Zimmermann A, Bleifuss E, Hengel H. Identification of DNA-damage
845 DNA-binding protein 1 as a conditional essential factor for cytomegalovirus replication in interferon-gamma-
846 stimulated cells. PLoS pathogens. 2011;7(6):e1002069. doi: 10.1371/journal.ppat.1002069.
847 21. Paradkar PN, Duchemin JB, Rodriguez-Andres J, Trinidad L, Walker PJ. Cullin4 Is Pro-Viral during
848 West Nile Virus Infection of Culex Mosquitoes. PLoS pathogens. 2015;11(9):e1005143. doi:
849 10.1371/journal.ppat.1005143.
850 22. Decorsiere A, Mueller H, van Breugel PC, Abdul F, Gerossier L, Beran RK, et al. Hepatitis B virus X
851 protein identifies the Smc5/6 complex as a host restriction factor. Nature. 2016;531(7594):386-9. doi:
852 10.1038/nature17170.
853 23. Murphy CM, Xu Y, Li F, Nio K, Reszka-Blanco N, Li X, et al. Hepatitis B Virus X Protein Promotes
854 Degradation of SMC5/6 to Enhance HBV Replication. Cell reports. 2016;16(11):2846-54. doi:
855 10.1016/j.celrep.2016.08.026.

856 24. Lim ES, Fregoso OI, McCoy CO, Matsen FA, Malik HS, Emerman M. The ability of primate
857 lentiviruses to degrade the monocyte restriction factor SAMHD1 preceded the birth of the viral accessory protein
858 Vpx. Cell host & microbe. 2012;11(2):194-204. Epub 2012/01/31. doi: 10.1016/j.chom.2012.01.004.
859 25. Romani B, Cohen EA. Lentivirus Vpr and Vpx accessory proteins usurp the cullin4-DDB1 (DCAF1)
860 E3 ubiquitin ligase. Current opinion in virology. 2012;2(6):755-63. Epub 2012/10/16. doi:
861 10.1016/j.coviro.2012.09.010.
862 26. Fabryova H, Strebel K. Vpr and Its Cellular Interaction Partners: R We There Yet? Cells. 2019;8(11).
863 doi: 10.3390/cells8111310.
864 27. Greenwood EJD, Williamson JC, Sienkiewicz A, Naamati A, Matheson NJ, Lehner PJ. Promiscuous
865 Targeting of Cellular Proteins by Vpr Drives Systems-Level Proteomic Remodeling in HIV-1 Infection. Cell
866 reports. 2019;27(5):1579-96 e7. doi: 10.1016/j.celrep.2019.04.025.
867 28. Schrofelbauer B, Yu Q, Zeitlin SG, Landau NR. Human immunodeficiency virus type 1 Vpr induces the
868 degradation of the UNG and SMUG uracil-DNA glycosylases. Journal of virology. 2005;79(17):10978-87. doi:
869 10.1128/JVI.79.17.10978-10987.2005.
870 29. Lahouassa H, Blondot ML, Chauveau L, Chougui G, Morel M, Leduc M, et al. HIV-1 Vpr degrades the
871 HLTF DNA translocase in T cells and macrophages. Proceedings of the National Academy of Sciences of the
872 United States of America. 2016;113(19):5311-6. doi: 10.1073/pnas.1600485113.
873 30. Laguette N, Bregnard C, Hue P, Basbous J, Yatim A, Larroque M, et al. Premature activation of the
874 SLX4 complex by Vpr promotes G2/M arrest and escape from innate immune sensing. Cell. 2014;156(1-2):134-
875 45. Epub 2014/01/15. doi: 10.1016/j.cell.2013.12.011.
876 31. Zhou X, DeLucia M, Ahn J. SLX4-SLX1 Protein-independent Down-regulation of MUS81-EME1
877 Protein by HIV-1 Viral Protein R (Vpr). The Journal of biological chemistry. 2016;291(33):16936-47. doi:
878 10.1074/jbc.M116.721183.
879 32. Romani B, Shaykh Baygloo N, Aghasadeghi MR, Allahbakhshi E. HIV-1 Vpr Protein Enhances
880 Proteasomal Degradation of MCM10 DNA Replication Factor through the Cul4-DDB1[VprBP] E3 Ubiquitin
881 Ligase to Induce G2/M Cell Cycle Arrest. The Journal of biological chemistry. 2015;290(28):17380-9. doi:
882 10.1074/jbc.M115.641522.
883 33. Lv L, Wang Q, Xu Y, Tsao LC, Nakagawa T, Guo H, et al. Vpr Targets TET2 for Degradation by
884 CRL4(VprBP) E3 Ligase to Sustain IL-6 Expression and Enhance HIV-1 Replication. Molecular cell.
885 2018;70(5):961-70 e5. doi: 10.1016/j.molcel.2018.05.007.

886 34. Su J, Rui Y, Lou M, Yin L, Xiong H, Zhou Z, et al. HIV-2/SIV Vpx targets a novel functional domain
887 of STING to selectively inhibit cGAS-STING-mediated NF-kappaB signalling. Nat Microbiol. 2019;4(12):2552-
888 64. doi: 10.1038/s41564-019-0585-4.
889 35. Chougui G, Munir-Matloob S, Matkovic R, Martin MM, Morel M, Lahouassa H, et al. HIV-2/SIV viral
890 protein X counteracts HUSH repressor complex. Nat Microbiol. 2018;3(8):891-7. doi: 10.1038/s41564-018-
891 0179-6.
892 36. Yurkovetskiy L, Guney MH, Kim K, Goh SL, McCauley S, Dauphin A, et al. Primate
893 immunodeficiency virus proteins Vpx and Vpr counteract transcriptional repression of proviruses by the HUSH
894 complex. Nat Microbiol. 2018;3(12):1354-61. doi: 10.1038/s41564-018-0256-x.
895 37. Hrecka K, Hao C, Gierszewska M, Swanson SK, Kesik-Brodacka M, Srivastava S, et al. Vpx relieves
896 inhibition of HIV-1 infection of macrophages mediated by the SAMHD1 protein. Nature. 2011;474(7353):658-
897 61. Epub 2011/07/02. doi: 10.1038/nature10195.
898 38. Laguette N, Sobhian B, Casartelli N, Ringeard M, Chable-Bessia C, Segeral E, et al. SAMHD1 is the
899 dendritic- and myeloid-cell-specific HIV-1 restriction factor counteracted by Vpx. Nature. 2011;474(7353):654-
900 7. Epub 2011/05/27. doi: 10.1038/nature10117.
901 39. Powell RD, Holland PJ, Hollis T, Perrino FW. Aicardi-Goutieres syndrome gene and HIV-1 restriction
902 factor SAMHD1 is a dGTP-regulated deoxynucleotide triphosphohydrolase. The Journal of biological chemistry.
903 2011;286(51):43596-600. Epub 2011/11/10. doi: 10.1074/jbc.C111.317628.
904 40. Goldstone DC, Ennis-Adeniran V, Hedden JJ, Groom HC, Rice GI, Christodoulou E, et al. HIV-1
905 restriction factor SAMHD1 is a deoxynucleoside triphosphate triphosphohydrolase. Nature.
906 2011;480(7377):379-82. Epub 2011/11/08. doi: 10.1038/nature10623.
907 41. Zhu C, Gao W, Zhao K, Qin X, Zhang Y, Peng X, et al. Structural insight into dGTP-dependent
908 activation of tetrameric SAMHD1 deoxynucleoside triphosphate triphosphohydrolase. Nature communications.
909 2013;4:2722. Epub 2013/11/13. doi: 10.1038/ncomms3722.
910 42. Kim B, Nguyen LA, Daddacha W, Hollenbaugh JA. Tight interplay among SAMHD1 protein level,
911 cellular dNTP levels, and HIV-1 proviral DNA synthesis kinetics in human primary monocyte-derived
912 macrophages. The Journal of biological chemistry. 2012;287(26):21570-4. Epub 2012/05/17. doi:
913 10.1074/jbc.C112.374843.
914 43. Lahouassa H, Daddacha W, Hofmann H, Ayinde D, Logue EC, Dragin L, et al. SAMHD1 restricts the
915 replication of human immunodeficiency virus type 1 by depleting the intracellular pool of deoxynucleoside
916 triphosphates. Nature immunology. 2012;13(3):223-8. Epub 2012/02/14. doi: 10.1038/ni.2236.

917 44. St Gelais C, de Silva S, Amie SM, Coleman CM, Hoy H, Hollenbaugh JA, et al. SAMHD1 restricts
918 HIV-1 infection in dendritic cells (DCs) by dNTP depletion, but its expression in DCs and primary CD4+ T-
919 lymphocytes cannot be upregulated by interferons. Retrovirology. 2012;9:105. Epub 2012/12/13. doi:
920 10.1186/1742-4690-9-105.
921 45. Rehwinkel J, Maelfait J, Bridgeman A, Rigby R, Hayward B, Liberatore RA, et al. SAMHD1-
922 dependent retroviral control and escape in mice. The EMBO journal. 2013;32(18):2454-62. Epub 2013/07/23.
923 doi: 10.1038/emboj.2013.163.
924 46. Morris ER, Taylor IA. The missing link: allostery and catalysis in the anti-viral protein SAMHD1.
925 Biochem Soc Trans. 2019;47(4):1013-27. doi: 10.1042/BST20180348.
926 47. Baldauf HM, Pan X, Erikson E, Schmidt S, Daddacha W, Burggraf M, et al. SAMHD1 restricts HIV-1
927 infection in resting CD4(+) T cells. Nature medicine. 2012;18(11):1682-7. Epub 2012/09/14. doi:
928 10.1038/nm.2964.
929 48. Shingai M, Welbourn S, Brenchley JM, Acharya P, Miyagi E, Plishka RJ, et al. The Expression of
930 Functional Vpx during Pathogenic SIVmac Infections of Rhesus Macaques Suppresses SAMHD1 in CD4+
931 Memory T Cells. PLoS pathogens. 2015;11(5):e1004928. doi: 10.1371/journal.ppat.1004928.
932 49. Fregoso OI, Ahn J, Wang C, Mehrens J, Skowronski J, Emerman M. Evolutionary toggling of Vpx/Vpr
933 specificity results in divergent recognition of the restriction factor SAMHD1. PLoS pathogens.
934 2013;9(7):e1003496. Epub 2013/07/23. doi: 10.1371/journal.ppat.1003496.
935 50. Schwefel D, Groom HC, Boucherit VC, Christodoulou E, Walker PA, Stoye JP, et al. Structural basis of
936 lentiviral subversion of a cellular protein degradation pathway. Nature. 2014;505(7482):234-8. Epub 2013/12/18.
937 doi: 10.1038/nature12815.
938 51. Schwefel D, Boucherit VC, Christodoulou E, Walker PA, Stoye JP, Bishop KN, et al. Molecular
939 Determinants for Recognition of Divergent SAMHD1 Proteins by the Lentiviral Accessory Protein Vpx. Cell
940 host & microbe. 2015;17(4):489-99. Epub 2015/04/10. doi: 10.1016/j.chom.2015.03.004.
941 52. Wu Y, Koharudin LM, Mehrens J, DeLucia M, Byeon CH, Byeon IJ, et al. Structural Basis of Clade-
942 specific Engagement of SAMHD1 (Sterile alpha Motif and Histidine/Aspartate-containing Protein 1) Restriction
943 Factors by Lentiviral Viral Protein X (Vpx) Virulence Factors. The Journal of biological chemistry.
944 2015;290(29):17935-45. doi: 10.1074/jbc.M115.665513.
945 53. Spragg CJ, Emerman M. Antagonism of SAMHD1 is actively maintained in natural infections of simian
946 immunodeficiency virus. Proceedings of the National Academy of Sciences of the United States of America.
947 2013;110(52):21136-41. Epub 2013/12/11. doi: 10.1073/pnas.1316839110.

948 54. Wu Y, Zhou X, Barnes CO, DeLucia M, Cohen AE, Gronenborn AM, et al. The DDB1-DCAF1-Vpr-
949 UNG2 crystal structure reveals how HIV-1 Vpr steers human UNG2 toward destruction. Nature structural &
950 molecular biology. 2016;23(10):933-40. doi: 10.1038/nsmb.3284.
951 55. Enchev RI, Schulman BA, Peter M. Protein neddylation: beyond cullin-RING ligases. Nature reviews
952 Molecular cell biology. 2015;16(1):30-44. doi: 10.1038/nrm3919.
953 56. Duda DM, Borg LA, Scott DC, Hunt HW, Hammel M, Schulman BA. Structural insights into NEDD8
954 activation of cullin-RING ligases: conformational control of conjugation. Cell. 2008;134(6):995-1006. doi:
955 10.1016/j.cell.2008.07.022.
956 57. Fischer ES, Bohm K, Lydeard JR, Yang H, Stadler MB, Cavadini S, et al. Structure of the DDB1-
957 CRBN E3 ubiquitin ligase in complex with thalidomide. Nature. 2014;512(7512):49-53. doi:
958 10.1038/nature13527.
959 58. Schneider M, Belsom A, Rappsilber J. Protein Tertiary Structure by Crosslinking/Mass Spectrometry.
960 Trends in biochemical sciences. 2018;43(3):157-69. Epub 2018/02/06. doi: 10.1016/j.tibs.2017.12.006.
961 59. O'Reilly FJ, Rappsilber J. Cross-linking mass spectrometry: methods and applications in structural,
962 molecular and systems biology. Nature structural & molecular biology. 2018;25(11):1000-8. Epub 2018/10/31.
963 doi: 10.1038/s41594-018-0147-0.
964 60. van Zundert GC, Bonvin AM. DisVis: quantifying and visualizing accessible interaction space of
965 distance-restrained biomolecular complexes. Bioinformatics. 2015;31(19):3222-4. Epub 2015/05/31. doi:
966 10.1093/bioinformatics/btv333.
967 61. van Zundert GC, Trellet M, Schaarschmidt J, Kurkcuoglu Z, David M, Verlato M, et al. The DisVis and
968 PowerFit Web Servers: Explorative and Integrative Modeling of Biomolecular Complexes. Journal of molecular
969 biology. 2017;429(3):399-407. Epub 2016/12/13. doi: 10.1016/j.jmb.2016.11.032.
970 62. DeLucia M, Mehrens J, Wu Y, Ahn J. HIV-2 and SIVmac accessory virulence factor Vpx down-
971 regulates SAMHD1 enzyme catalysis prior to proteasome-dependent degradation. The Journal of biological
972 chemistry. 2013;288(26):19116-26. doi: 10.1074/jbc.M113.469007.
973 63. Yan J, Kaur S, DeLucia M, Hao C, Mehrens J, Wang C, et al. Tetramerization of SAMHD1 is required
974 for biological activity and inhibition of HIV infection. The Journal of biological chemistry. 2013;288(15):10406-
975 17. Epub 2013/02/22. doi: 10.1074/jbc.M112.443796.
976 64. Arnold LH, Groom HC, Kunzelmann S, Schwefel D, Caswell SJ, Ordonez P, et al. Phospho-dependent
977 Regulation of SAMHD1 Oligomerisation Couples Catalysis and Restriction. PLoS pathogens.
978 2015;11(10):e1005194. Epub 2015/10/03. doi: 10.1371/journal.ppat.1005194.

979 65. Yan J, Hao C, DeLucia M, Swanson S, Florens L, Washburn MP, et al. CyclinA2-Cyclin-dependent
980 Kinase Regulates SAMHD1 Protein Phosphohydrolase Domain. The Journal of biological chemistry.
981 2015;290(21):13279-92. Epub 2015/04/08. doi: 10.1074/jbc.M115.646588.
982 66. Berger G, Lawrence M, Hue S, Neil SJ. G2/M cell cycle arrest correlates with primate lentiviral Vpr
983 interaction with the SLX4 complex. Journal of virology. 2014. Epub 2014/10/17. doi: 10.1128/JVI.02307-14.
984 67. Daugherty MD, Malik HS. Rules of engagement: molecular insights from host-virus arms races. Annual
985 review of genetics. 2012;46:677-700. Epub 2012/11/14. doi: 10.1146/annurev-genet-110711-155522.
986 68. Duggal NK, Emerman M. Evolutionary conflicts between viruses and restriction factors shape
987 immunity. Nat Rev Immunol. 2012;12(10):687-95. Epub 2012/09/15. doi: 10.1038/nri3295.
988 69. Uriu K, Kosugi Y, Ito J, Sato K. The Battle between Retroviruses and APOBEC3 Genes: Its Past and
989 Present. Viruses. 2021;13(1). Epub 2021/01/23. doi: 10.3390/v13010124.
990 70. Guenzel CA, Herate C, Benichou S. HIV-1 Vpr-a still "enigmatic multitasker". Front Microbiol.
991 2014;5:127. doi: 10.3389/fmicb.2014.00127.
992 71. Stivahtis GL, Soares MA, Vodicka MA, Hahn BH, Emerman M. Conservation and host specificity of
993 Vpr-mediated cell cycle arrest suggest a fundamental role in primate lentivirus evolution and biology. Journal of
994 virology. 1997;71(6):4331-8.
995 72. Planelles V, Jowett JB, Li QX, Xie Y, Hahn B, Chen IS. Vpr-induced cell cycle arrest is conserved
996 among primate lentiviruses. Journal of virology. 1996;70(4):2516-24.
997 73. Baek K, Krist DT, Prabu JR, Hill S, Klugel M, Neumaier LM, et al. NEDD8 nucleates a multivalent
998 cullin-RING-UBE2D ubiquitin ligation assembly. Nature. 2020;578(7795):461-6. doi: 10.1038/s41586-020-
999 2000-y.
1000 74. Schapira M, Calabrese MF, Bullock AN, Crews CM. Targeted protein degradation: expanding the
1001 toolbox. Nat Rev Drug Discov. 2019;18(12):949-63. doi: 10.1038/s41573-019-0047-y.
1002 75. Hanzl A, Winter GE. Targeted protein degradation: current and future challenges. Curr Opin Chem
1003 Biol. 2020;56:35-41. doi: 10.1016/j.cbpa.2019.11.012.
1004 76. Antiretroviral Therapy Cohort C. Life expectancy of individuals on combination antiretroviral therapy
1005 in high-income countries: a collaborative analysis of 14 cohort studies. Lancet. 2008;372(9635):293-9. Epub
1006 2008/07/29. doi: 10.1016/S0140-6736(08)61113-7.
1007 77. Gunthard HF, Calvez V, Paredes R, Pillay D, Shafer RW, Wensing AM, et al. Human
1008 Immunodeficiency Virus Drug Resistance: 2018 Recommendations of the International Antiviral Society-USA
1009 Panel. Clin Infect Dis. 2019;68(2):177-87. Epub 2018/07/28. doi: 10.1093/cid/ciy463.

1010 78. Miller RH, Sarver N. HIV accessory proteins as therapeutic targets. Nature medicine. 1997;3(4):389-94.
1011 Epub 1997/04/01. doi: 10.1038/nm0497-389.
1012 79. Puhl AC, Garzino Demo A, Makarov VA, Ekins S. New targets for HIV drug discovery. Drug Discov
1013 Today. 2019;24(5):1139-47. Epub 2019/03/20. doi: 10.1016/j.drudis.2019.03.013.
1014 80. Nathans R, Cao H, Sharova N, Ali A, Sharkey M, Stranska R, et al. Small-molecule inhibition of HIV-1
1015 Vif. Nat Biotechnol. 2008;26(10):1187-92. Epub 2008/09/23. doi: 10.1038/nbt.1496.
1016 81. Zuo T, Liu D, Lv W, Wang X, Wang J, Lv M, et al. Small-molecule inhibition of human
1017 immunodeficiency virus type 1 replication by targeting the interaction between Vif and ElonginC. Journal of
1018 virology. 2012;86(10):5497-507. Epub 2012/03/02. doi: 10.1128/JVI.06957-11.
1019 82. Ma L, Zhang Z, Liu Z, Pan Q, Wang J, Li X, et al. Identification of small molecule compounds
1020 targeting the interaction of HIV-1 Vif and human APOBEC3G by virtual screening and biological evaluation.
1021 Scientific reports. 2018;8(1):8067. Epub 2018/05/26. doi: 10.1038/s41598-018-26318-3.
1022 83. Gonzalez ME. The HIV-1 Vpr Protein: A Multifaceted Target for Therapeutic Intervention. Int J Mol
1023 Sci. 2017;18(1). Epub 2017/01/12. doi: 10.3390/ijms18010126.
1024 84. Zhao Y, Chapman DA, Jones IM. Improving baculovirus recombination. Nucleic acids research.
1025 2003;31(2):E6-. Epub 2003/01/16.
1026 85. Wilkins MR, Gasteiger E, Bairoch A, Sanchez JC, Williams KL, Appel RD, et al. Protein identification
1027 and analysis tools in the ExPASy server. Methods Mol Biol. 1999;112:531-52. Epub 1999/02/23. doi: 10.1385/1-
1028 59259-584-7:531.
1029 86. Kabsch W. Xds. Acta crystallographica Section D, Biological crystallography. 2010;66(Pt 2):125-32.
1030 Epub 2010/02/04. doi: 10.1107/S0907444909047337.
1031 87. Vagin A, Teplyakov A. Molecular replacement with MOLREP. Acta crystallographica Section D,
1032 Biological crystallography. 2010;66(Pt 1):22-5. Epub 2010/01/09. doi: 10.1107/S0907444909042589.
1033 88. Emsley P, Cowtan K. Coot: model-building tools for molecular graphics. Acta crystallographica Section
1034 D, Biological crystallography. 2004;60(Pt 12 Pt 1):2126-32. Epub 2004/12/02. doi:
1035 10.1107/S0907444904019158.
1036 89. Liebschner D, Afonine PV, Baker ML, Bunkoczi G, Chen VB, Croll TI, et al. Macromolecular structure
1037 determination using X-rays, neutrons and electrons: recent developments in Phenix. Acta Crystallogr D Struct
1038 Biol. 2019;75(Pt 10):861-77. Epub 2019/10/08. doi: 10.1107/S2059798319011471.
1039 90. Sparta KM, Krug M, Heinemann U, Mueller U, Weiss MS. XDSAPP2.0. Journal of Applied
1040 Crystallography. 2016;49(3):1085-92. doi: doi:10.1107/S1600576716004416.

1041 91. McCoy AJ, Grosse-Kunstleve RW, Adams PD, Winn MD, Storoni LC, Read RJ. Phaser
1042 crystallographic software. Journal of Applied Crystallography. 2007;40(4):658-74. doi:
1043 doi:10.1107/S0021889807021206.
1044 92. Kuroki R, Weaver LH, Matthews BW. Structural basis of the conversion of T4 lysozyme into a
1045 transglycosidase by reengineering the active site. Proceedings of the National Academy of Sciences of the
1046 United States of America. 1999;96(16):8949-54. Epub 1999/08/04. doi: 10.1073/pnas.96.16.8949.
1047 93. Morellet N, Bouaziz S, Petitjean P, Roques BP. NMR structure of the HIV-1 regulatory protein VPR.
1048 Journal of molecular biology. 2003;327(1):215-27. Epub 2003/03/05.
1049 94. Carragher B, Kisseberth N, Kriegman D, Milligan RA, Potter CS, Pulokas J, et al. Leginon: an
1050 automated system for acquisition of images from vitreous ice specimens. J Struct Biol. 2000;132(1):33-45. Epub
1051 2000/12/21. doi: 10.1006/jsbi.2000.4314.
1052 95. Suloway C, Pulokas J, Fellmann D, Cheng A, Guerra F, Quispe J, et al. Automated molecular
1053 microscopy: the new Leginon system. J Struct Biol. 2005;151(1):41-60. Epub 2005/05/14. doi:
1054 10.1016/j.jsb.2005.03.010.
1055 96. Moriya T, Saur M, Stabrin M, Merino F, Voicu H, Huang Z, et al. High-resolution Single Particle
1056 Analysis from Electron Cryo-microscopy Images Using SPHIRE. J Vis Exp. 2017;(123). Epub 2017/06/02. doi:
1057 10.3791/55448.
1058 97. Grant T, Rohou A, Grigorieff N. cisTEM, user-friendly software for single-particle image processing.
1059 Elife. 2018;7. Epub 2018/03/08. doi: 10.7554/eLife.35383.
1060 98. Zivanov J, Nakane T, Forsberg BO, Kimanius D, Hagen WJ, Lindahl E, et al. New tools for automated
1061 high-resolution cryo-EM structure determination in RELION-3. Elife. 2018;7. Epub 2018/11/10. doi:
1062 10.7554/eLife.42166.
1063 99. Zheng SQ, Palovcak E, Armache JP, Verba KA, Cheng Y, Agard DA. MotionCor2: anisotropic
1064 correction of beam-induced motion for improved cryo-electron microscopy. Nat Methods. 2017;14(4):331-2.
1065 Epub 2017/03/03. doi: 10.1038/nmeth.4193.
1066 100. Mindell JA, Grigorieff N. Accurate determination of local defocus and specimen tilt in electron
1067 microscopy. J Struct Biol. 2003;142(3):334-47. Epub 2003/06/05. doi: 10.1016/s1047-8477(03)00069-8.
1068 101. Pettersen EF, Goddard TD, Huang CC, Couch GS, Greenblatt DM, Meng EC, et al. UCSF Chimera--a
1069 visualization system for exploratory research and analysis. J Comput Chem. 2004;25(13):1605-12. Epub
1070 2004/07/21. doi: 10.1002/jcc.20084.

1071 102. Punjani A, Rubinstein JL, Fleet DJ, Brubaker MA. cryoSPARC: algorithms for rapid unsupervised
1072 cryo-EM structure determination. Nat Methods. 2017;14(3):290-6. Epub 2017/02/07. doi: 10.1038/nmeth.4169.
1073 103. Hayward S, Lee RA. Improvements in the analysis of domain motions in proteins from conformational
1074 change: DynDom version 1.50. J Mol Graph Model. 2002;21(3):181-3. Epub 2002/12/05. doi: 10.1016/s1093-
1075 3263(02)00140-7.
1076 104. Krissinel E, Henrick K. Inference of macromolecular assemblies from crystalline state. Journal of
1077 molecular biology. 2007;372(3):774-97. Epub 2007/08/08. doi: 10.1016/j.jmb.2007.05.022.
1078 105. Madeira F, Park YM, Lee J, Buso N, Gur T, Madhusoodanan N, et al. The EMBL-EBI search and
1079 sequence analysis tools APIs in 2019. Nucleic acids research. 2019;47(W1):W636-W41. Epub 2019/04/13. doi:
1080 10.1093/nar/gkz268.
1081 106. Nicholas KB, Nicholas Jr., H. B., Deerfield II., D. W. GeneDoc: Analysis and Visualization of Genetic
1082 Variation. embnetnews. 1997;4(2):1-4.
1083 107. Shevchenko A, Tomas H, Havlis J, Olsen JV, Mann M. In-gel digestion for mass spectrometric
1084 characterization of proteins and proteomes. Nature protocols. 2006;1(6):2856-60. Epub 2007/04/05. doi:
1085 10.1038/nprot.2006.468.
1086 108. Rappsilber J, Ishihama Y, Mann M. Stop and go extraction tips for matrix-assisted laser
1087 desorption/ionization, nanoelectrospray, and LC/MS sample pretreatment in proteomics. Anal Chem.
1088 2003;75(3):663-70. Epub 2003/02/15. doi: 10.1021/ac026117i.
1089 109. Kolbowski L, Mendes ML, Rappsilber J. Optimizing the Parameters Governing the Fragmentation of
1090 Cross-Linked Peptides in a Tribrid Mass Spectrometer. Anal Chem. 2017;89(10):5311-8. Epub 2017/04/14. doi:
1091 10.1021/acs.analchem.6b04935.
1092 110. Mendes ML, Fischer L, Chen ZA, Barbon M, O'Reilly FJ, Giese SH, et al. An integrated workflow for
1093 crosslinking mass spectrometry. Mol Syst Biol. 2019;15(9):e8994. Epub 2019/09/27. doi:
1094 10.15252/msb.20198994.
1095 111. Fischer L, Rappsilber J. Quirks of Error Estimation in Cross-Linking/Mass Spectrometry. Anal Chem.
1096 2017;89(7):3829-33. Epub 2017/03/08. doi: 10.1021/acs.analchem.6b03745.
1097 112. Yang J, Zhang Y. Protein Structure and Function Prediction Using I-TASSER. Curr Protoc
1098 Bioinformatics. 2015;52:5 8 1-5 8 15. Epub 2015/12/19. doi: 10.1002/0471250953.bi0508s52.
1099 113. Webb B, Sali A. Comparative Protein Structure Modeling Using MODELLER. Curr Protoc
1100 Bioinformatics. 2016;54:5 6 1-5 6 37. Epub 2016/06/21. doi: 10.1002/cpbi.3.

1101 114. Perez-Riverol Y, Csordas A, Bai J, Bernal-Llinares M, Hewapathirana S, Kundu DJ, et al. The PRIDE
1102 database and related tools and resources in 2019: improving support for quantification data. Nucleic acids
1103 research. 2019;47(D1):D442-D50. Epub 2018/11/06. doi: 10.1093/nar/gky1106.
1104 115. Shabek N, Ruble J, Waston CJ, Garbutt KC, Hinds TR, Li T, et al. Structural insights into DDA1
1105 function as a core component of the CRL4-DDB1 ubiquitin ligase. Cell Discov. 2018;4:67. Epub 2018/12/20.
1106 doi: 10.1038/s41421-018-0064-8.

1107

1108 # Figures

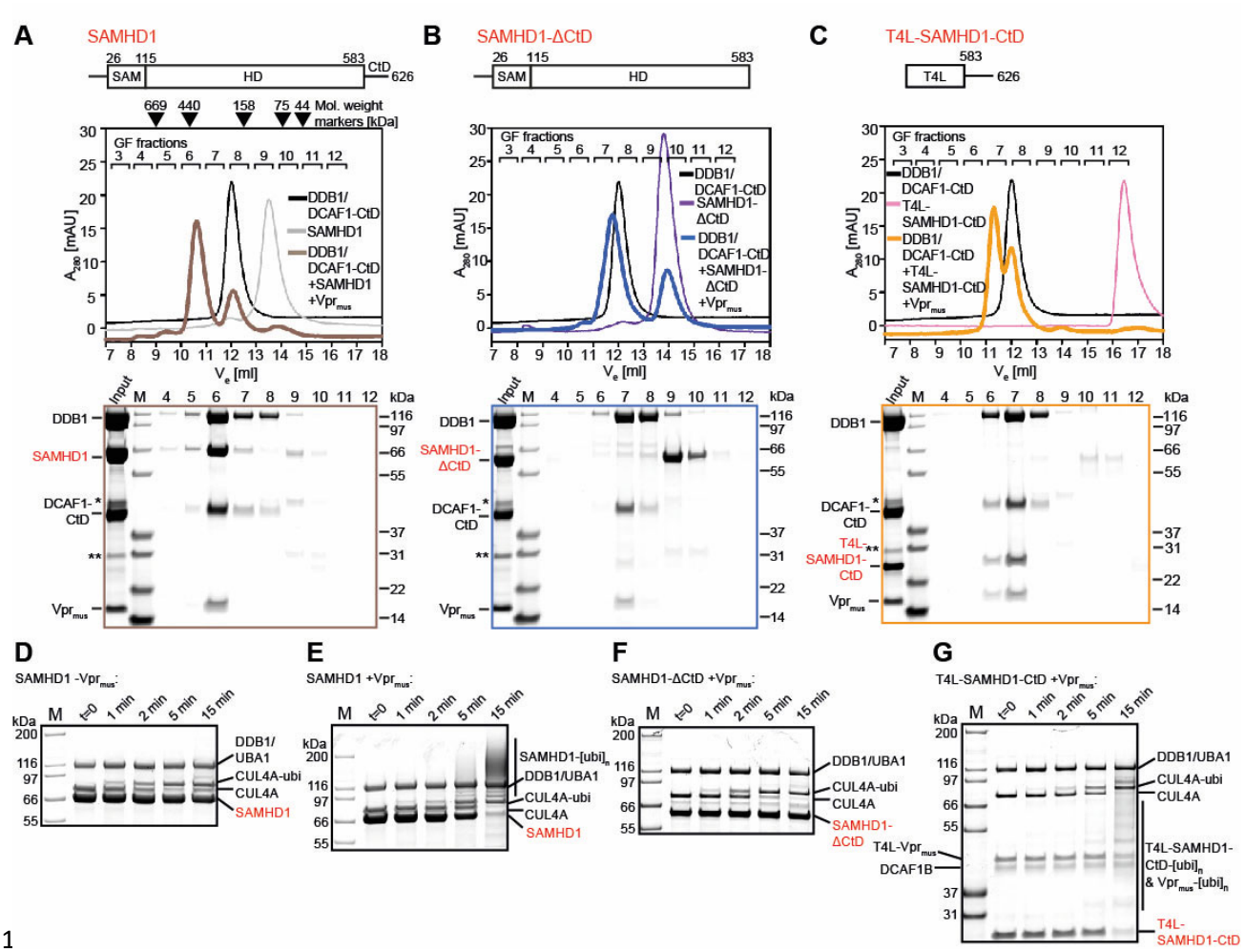


1

1110 **Fig 1. Biochemical analysis of Vpr$_{mus}$-induced CRL4$^{DCAF1}$ specificity redirection.**

1111 (**A-C**) GF analysis of *in vitro* reconstitution of protein complexes containing DDB1/DCAF1-CtD,
1112 Vpr$_{mus}$ and SAMHD1 (**A**), SAMHD1-ΔCtD (**B**) or T4L-SAMHD1-CtD (**C**). Elution volumes of protein
1113 molecular weight standards are indicated above the chromatogram in **A**. Coomassie blue-stained SDS-
1114 PAGE analyses of fractions collected during the GF runs are shown below the chromatograms, with
1115 boxes colour-coded with respect to the chromatograms. SAM – sterile α-motif domain, HD – histidine-
1116 aspartate domain, T4L – T4 Lysozyme. The asterisk and double asterisk indicate slight contaminations
1117 with remaining GST-3C protease and the GST purification tag, respectively. (**D-G**) *In vitro*
1118 ubiquitylation reactions with purified protein components in the absence (**D**) or presence (**E-G**) of
1119 Vpr$_{mus}$, with the indicated SAMHD1 constructs as substrate. Reactions were stopped after the indicated
1120 times, separated on SDS-PAGE and visualised by Coomassie blue staining.

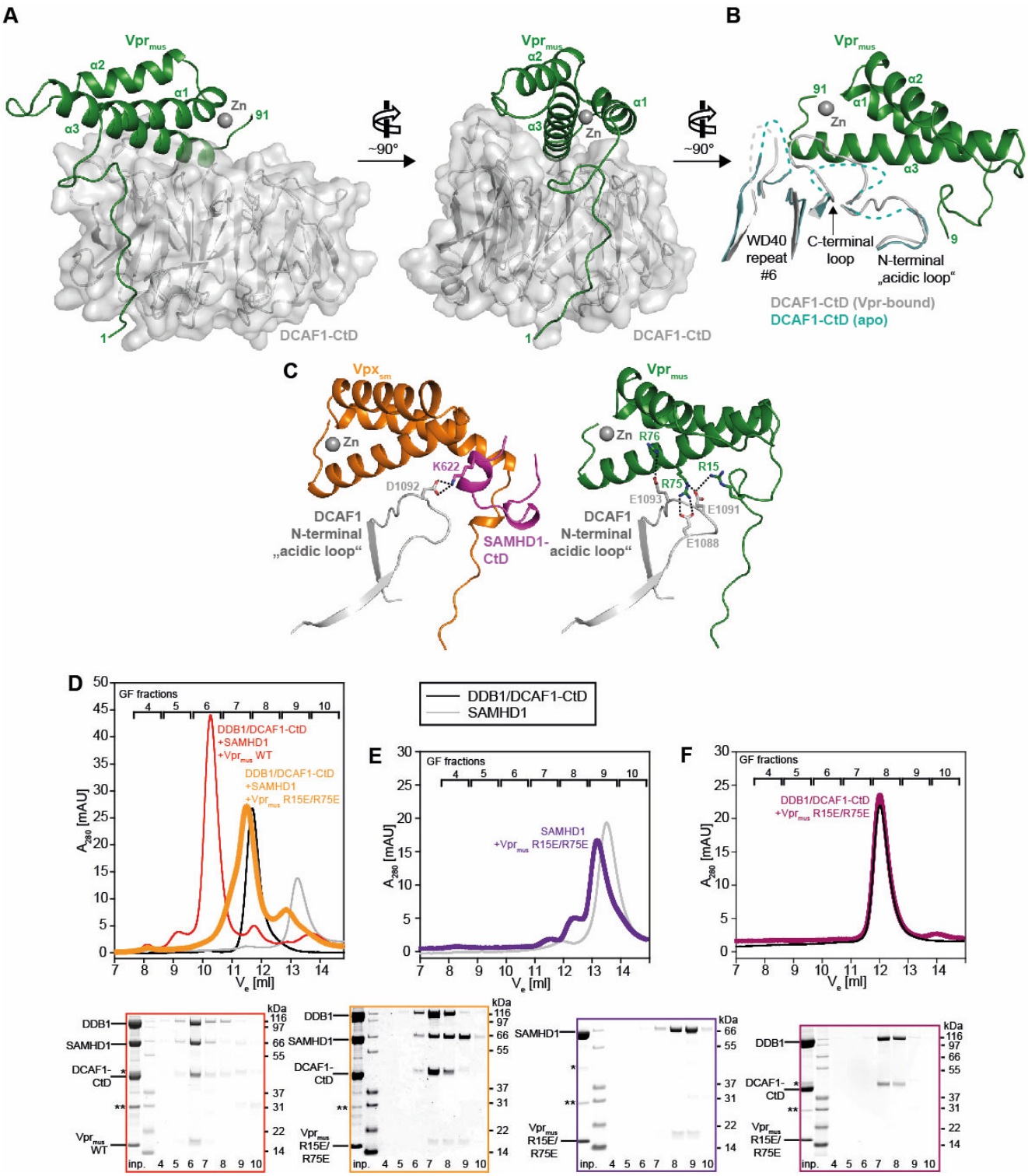


1122 **Fig 2. Crystal structure of the DDB1/DCAF1-CtD/Vpr$_{mus}$ complex.**

1123 (**A**) Overall structure of the DDB1/DCAF1-CtD/Vpr$_{mus}$ complex in two views. DCAF1-CtD is shown

1124 as grey cartoon and semi-transparent surface. Vpr$_{mus}$ is shown as a dark green cartoon with the co-

1125 ordinated zinc ion shown as grey sphere. T4L and DDB1 have been omitted for clarity. (**B**)

1126 Superposition of apo-DCAF1-CtD (light blue cartoon) with Vpr$_{mus}$-bound DCAF1-CtD (grey/green

1127 cartoon). Only DCAF1-CtD regions with significant structural differences between apo- and $Vpr_{mus}$-
1128 bound forms are shown. Disordered loops are indicated as dashed lines. (**C**) Comparison of the binary
1129 $Vpr_{mus}$/DCAF1-CtD and ternary $Vpx_{sm}$/DCAF1-CtD/SAMHD1-CtD complexes. For DCAF1-CtD, only
1130 the N-terminal "acidic loop" region is shown. $Vpr_{mus}$, DCAF1-CtD and bound zinc are coloured as in
1131 **A**; $Vpx_{sm}$ is represented as orange cartoon and SAMHD1-CtD as pink cartoon. Selected
1132 Vpr/Vpx/DCAF1-CtD side chains are shown as sticks, and electrostatic interactions between these side
1133 chains are indicated as dotted lines. (**D**) GF analysis of *in vitro* reconstitution of protein complexes
1134 containing DDB1/DCAF1-CtD/$Vpr_{mus}$ or the $Vpr_{mus}$ R15E/R75E mutant, and SAMHD1. SDS-PAGE
1135 analyses of corresponding GF fractions are shown below the chromatogram, with boxes colour-coded
1136 with respect to the chromatogram. (**E-F**) *In vitro* reconstitution of protein complexes containing
1137 SAMHD1 and $Vpr_{mus}$ R15E/R75E (**E**) or DDB1/DCAF1-CtD and $Vpr_{mus}$ R15E/R75E (**F**). SDS-PAGE
1138 analyses of corresponding GF fractions are shown below the chromatogram, with boxes colour-coded
1139 with respect to the chromatogram. The asterisk and double asterisk indicate slight contaminations with
1140 remaining GST-3C protease and the GST purification tag, respectively.

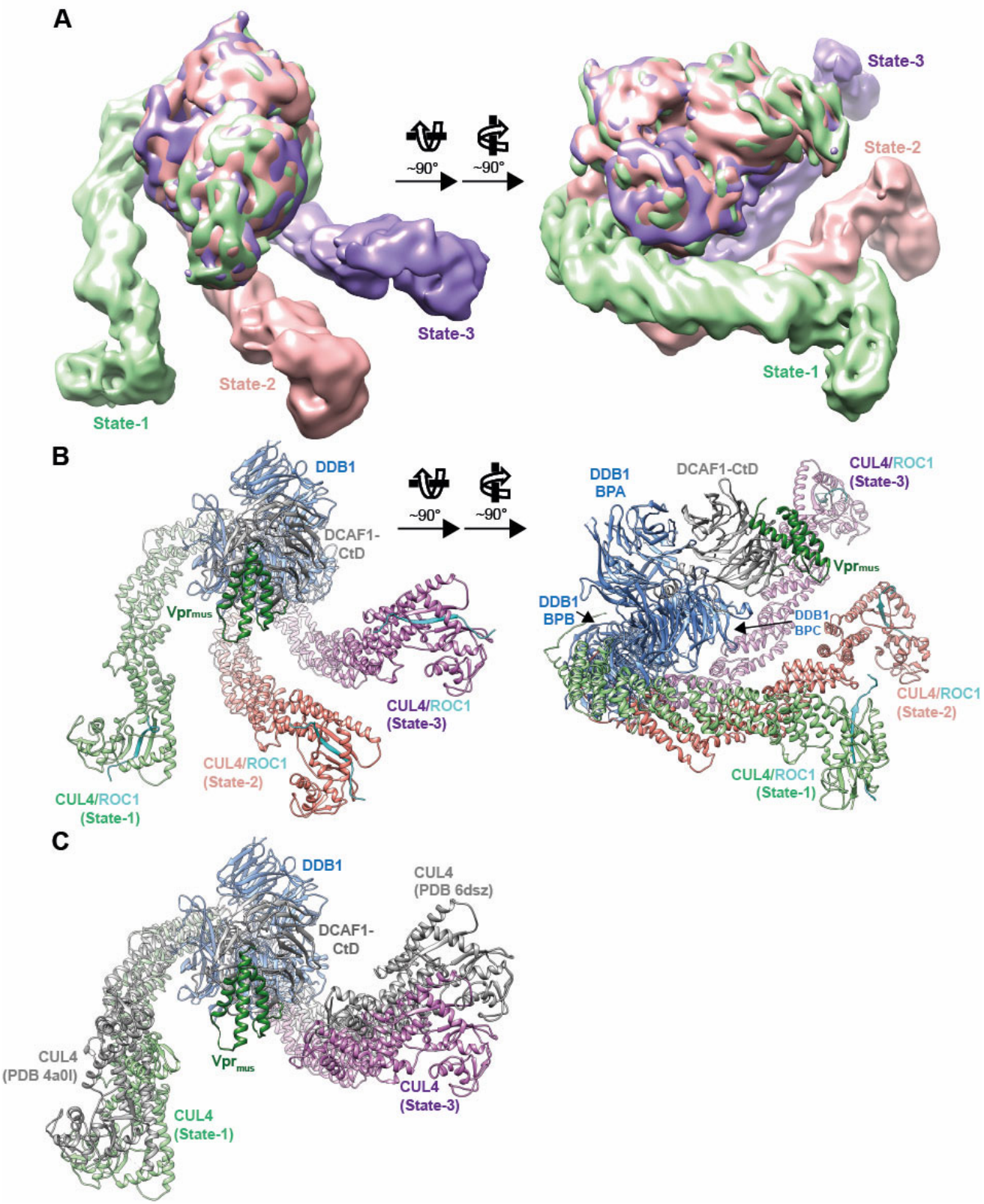


1142 **Fig 3. Cryo-EM analysis of CRL4-NEDD8$^{DCAF1\text{-}CtD}$/Vpr$_{mus}$/SAMHD1 conformational states.**

1143 (**A**) Two views of an overlay of CRL4-NEDD8$^{DCAF1\text{-}CtD}$/Vpr$_{mus}$/SAMHD1 cryo-EM reconstructions

1144 (conformational state-1 – light green, state-2 – salmon, state-3 – purple). The portions of the densities

1145 corresponding to DDB1 BPA/BPC, DCAF1-CtD and Vpr$_{mus}$ have been superimposed. (**B**) Two views

1146 of a superposition of DDB1/DCAF1-CtD/$Vpr_{mus}$ and CUL4/ROC1 (PDB 2hye) [15] molecular models,
1147 which have been fitted as rigid bodies to the corresponding cryo-EM densities; the models are oriented
1148 as in **A**. DDB1/DCAF1-CtD/$Vpr_{mus}$ is shown as in Fig 2A, CUL4 is shown as cartoon, coloured as in **A**
1149 and ROC1 is shown as cyan cartoon. (**C**) Comparison of outermost CUL4 stalk orientations observed
1150 in the cryo-EM analysis presented here (states-1 and -3, coloured as in **B**, show 119.5° rotation of DDB1
1151 BPB) to the two most extreme stalk positions present in previous crystal structures (PDB 4a0l [13], PDB
1152 6dsz [115], coloured grey, show 143.4° DDB1 BPB rotation).

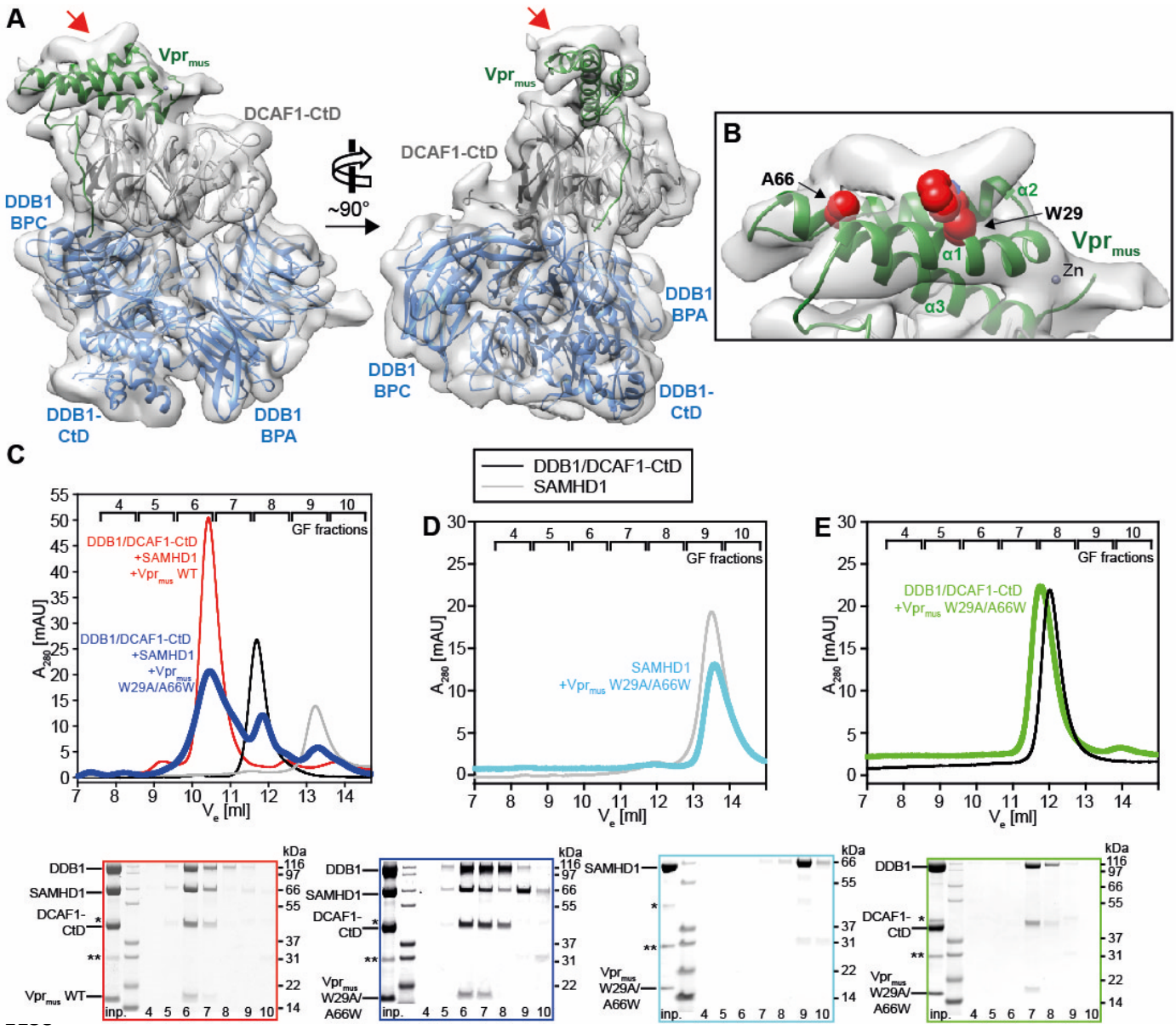


**Fig 4. Mechanism of SAMHD1-CtD recruitment by $Vpr_{mus}$.**

(**A**) Two views of the cryo-EM reconstruction of the CRL4-NEDD8$^{DCAF1\text{-}CtD}$/$Vpr_{mus}$/SAMHD1 core. The crystal structure of the DDB1/DCAF1-CtD/$Vpr_{mus}$ complex was fitted as a rigid body into the cryo-EM density and is shown in the same colours as in Fig 2A. The DDB1 BPB model and density was removed for clarity. The red arrows mark additional density on the upper surface of the $Vpr_{mus}$ helix bundle. (**B**) Detailed view of the SAMHD1-CtD electron density. The model is in the same orientation as in **A**, left panel. Selected $Vpr_{mus}$ residues W29 and A66, which are in close contact to the additional density, are shown as red space-fill representation. (**C**) *In vitro* reconstitution of protein complexes containing DDB1/DCAF1-CtD, $Vpr_{mus}$ or the $Vpr_{mus}$ W29A/A66W mutant, and SAMHD1, assessed by analytical GF. SDS-PAGE analyses of corresponding GF fractions are shown below the chromatogram,

1164 with boxes colour-coded with respect to the chromatogram. (**D-E**) *In vitro* reconstitution of protein
1165 complexes containing SAMHD1 and $Vpr_{mus}$ W29A/A66W (**D**) or DDB1/DCAF1-CtD and $Vpr_{mus}$
1166 W29A/A66W (**E**). SDS-PAGE analyses of corresponding GF fractions are shown below the
1167 chromatogram, with boxes colour-coded with respect to the chromatogram. The asterisk and double
1168 asterisk indicate slight contaminations with remaining GST-3C protease and the GST purification tag,
1169 respectively.

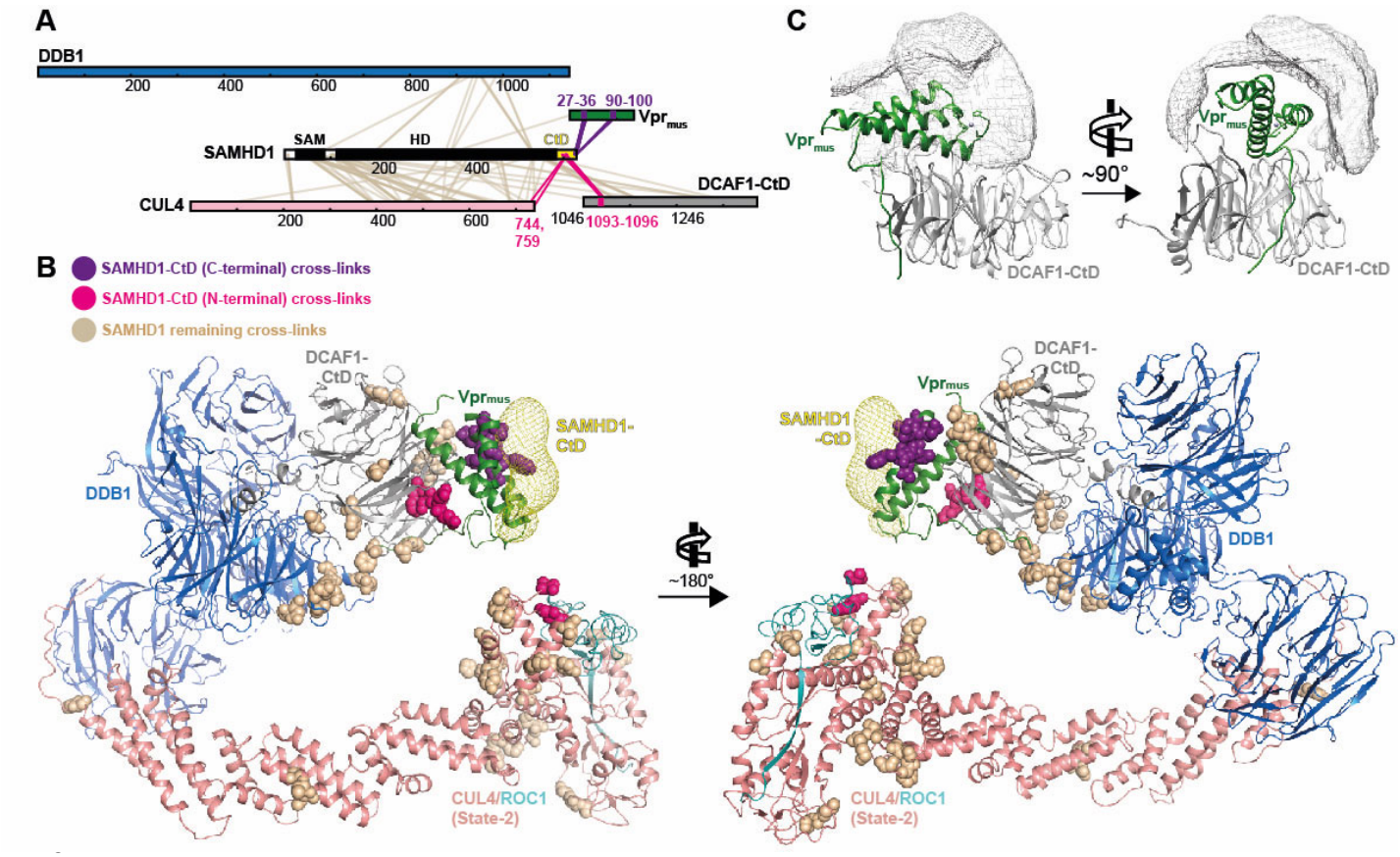


**Fig 5. Cross-linking mass spectrometry (CLMS) analysis of CRL4$^{DCAF1\text{-}CtD}$/ Vpr$_{mus}$/SAMHD1** (**A**) Schematic representation of sulfo-SDA cross-links between CRL4$^{DCAF1}$/Vpr$_{mus}$ and SAMHD1, identified by CLMS. Proteins are colour-coded as in Figs 3, 4, and SAMHD1 black/white. SAMHD1-CtD is highlighted in yellow. Crosslinks to the N-terminal SAMHD1 globular SAM and HD domains are coloured light brown, while cross-links to the N-terminal half of SAMHD1-CtD are highlighted in pink and cross-links to the C-terminal end of SAMHD1-CtD are coloured purple. (**B**) Sulfo-SDA cross-links from **A**, in the same colour scheme, mapped on the molecular model of CRL4-NEDD8$^{DCAF1\text{-}CtD}$/Vpr$_{mus}$/SAMHD1 (state-2), obtained from cryo-EM analysis (Fig 3). SAMHD1-CtD density from the CRL4-NEDD8$^{DCAF1\text{-}CtD}$/Vpr$_{mus}$/SAMHD1 (core) cryo-EM analysis (Fig. 4) is shown as yellow mesh. (**C**) The accessible interaction space of SAMHD1-CtD, calculated by the DisVis server [61], consistent with at least 14 of 26 observed cross-links, is visualised as grey mesh. DCAF1-CtD and Vpr$_{mus}$ are oriented and coloured as in Fig 4A.

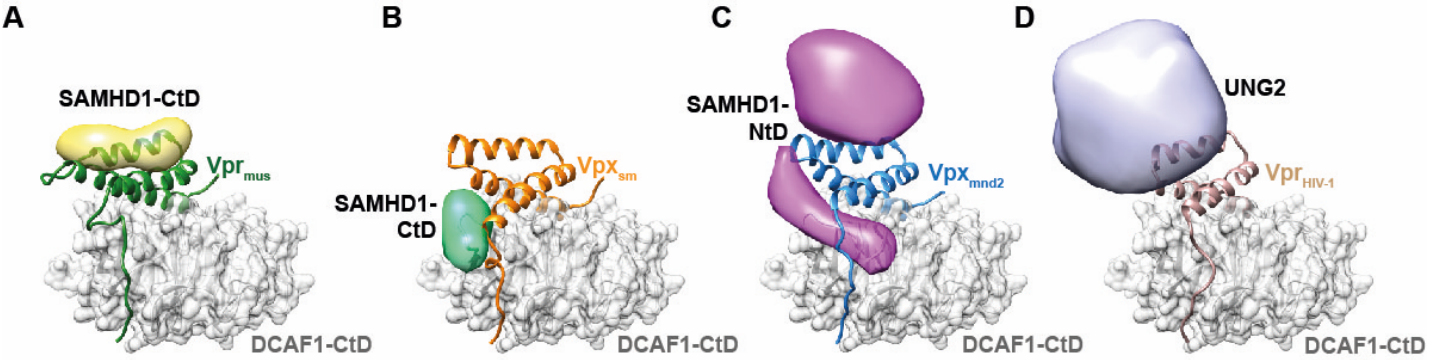


1184 **Fig 6. Variability of *neo*-substrate recognition in Vpx/Vpr proteins.**

1185 Comparison of *neo*-substrate recognition modes of $Vpr_{mus}$ (**A**), $Vpx_{sm}$ (**B**), $Vpx_{mnd2}$ (**C**) and $Vpr_{HIV-1}$ (**D**).
1186 DCAF1-CtD is shown as grey cartoon and semi-transparent surface, $Vpr_{mus}$ – green, $Vpx_{sm}$ – orange,
1187 $Vpx_{mnd2}$ – blue and $Vpr_{HIV-1}$– light brown are shown as cartoon. Models of the recruited ubiquitylation
1188 substrates are shown as strongly filtered, semi-transparent calculated electron density maps with the
1189 following colouring scheme: SAMHD1-CtD bound to $Vpr_{mus}$ – yellow, SAMHD1-CtD (bound to $Vpx_{sm}$,
1190 PDB 4cc9) [50] – mint green, SAMHD1-NtD ($Vpx_{mnd2}$, PDB 5aja) [51] – magenta, UNG2 ($Vpr_{HIV-1}$,
1191 PDB 5jk7) [54] – light violet.

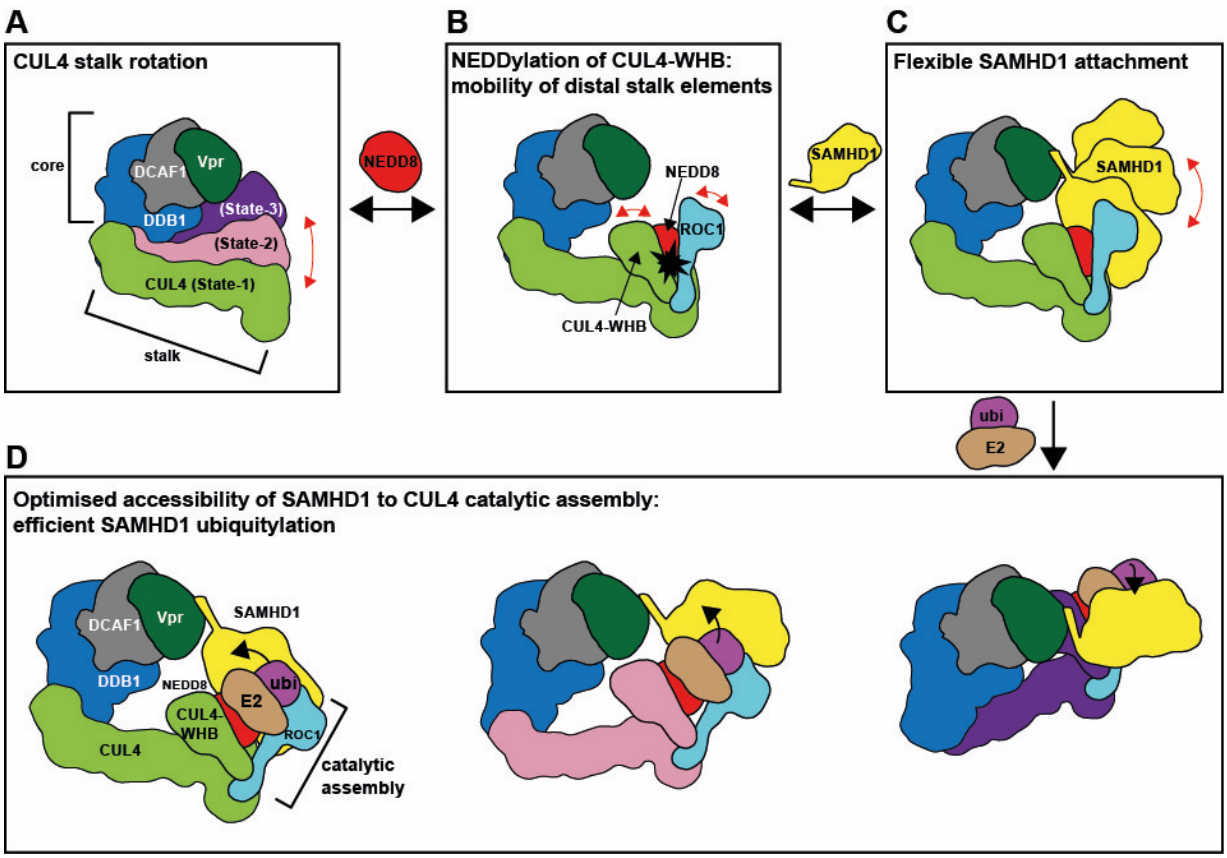


**Fig 7. Schematic illustration of structural plasticity in $Vpr_{mus}$-modified $CRL4^{DCAF1\text{-}CtD}$, and implications for ubiquitin transfer**.

(**A**) Rotation of the CRL4 stalk increases the space accessible to catalytic elements at the distal tip of the stalk, forming a ubiquitylation zone around the core. (**B**) Modification of CUL4-WHB with NEDD8 leads to increased mobility of these distal stalk elements (CUL4-WHB, ROC1 RING domain) [56], further extending the ubiquitylation zone and activating the formation of a catalytic assembly for ubiquitin transfer (see also **D**) [73]. (**C**) Flexible tethering of SAMHD1 to the core by $Vpr_{mus}$ places the bulk of SAMHD1 in the ubiquitylation zone and optimises surface accessibility. (**D**) Dynamic processes **A**-**C** together create numerous possibilities for assembly of the catalytic machinery (CUL4-NEDD8 WHB, ROC1, ubiquitin-(ubi-)charged E2) on surface-exposed SAMHD1 lysine side chains. Here, three of these possibilities are exemplified schematically. In this way, ubiquitin coverage on SAMHD1 is maximised.